Acid mine drainage sludge as an alternative raw material for M-type hexaferrite preparation

doi: 10.1016/j.jclepro.2019.03.224

Acid Mine Drainage Sludge as an Alternative Raw Material for M-type Hexaferrite Preparation

Mei Liu[a,b,*], Atsushi Iizuka[c], Etsuro Shibata[c]

[a]Graduate School of Environmental Studies, Tohoku University, Sendai 980-0845, Japan

[b]School of Material Science and Engineering, Jingdezhen Ceramic Institute, Jingdezhen 333403, China

[c]Institute of Multidisciplinary Research for Advanced Materials (IMRAM), Tohoku University, Sendai 980-8577, Japan

***Corresponding author**

*M. Liu: liu.mei.q5@dc.tohoku.ac.jp; maggieliujci@gmail.com

A. Iizuka: atsushi.iizuka.e4@tohoku.ac.jp

E. Shibata: etsuro.shibata.e3@tohoku.ac.jp

Abstract

Two types of dewatered acid mine drainage sludge were sampled from abandoned Japanese mines. The sludge shows great potential to be completely reused as alternative iron and calcium sources to synthesize M-type calcium substituted barium hexaferrite with addition of $BaCO_3$ by solid-state reaction. The precursors and as-prepared samples were investigated by X-ray diffraction (XRD), field-emission scanning electron microscopy, and thermogravimetry–mass spectroscopy. The effect of sludge addition on phase formation and microstructure evolution during calcination was discussed in details. For sludge content up to 93.9 mass % with addition of 6.1 mass % $BaCO_3$, M-type hexaferrite can be identified in the XRD patterns of as-prepared samples calcined at 1100, 1200, and 1300 °C. The impurities in the sludge, such as silicon, and aluminum, result in formation of secondary aluminosilicates phases; another impurity sulfur in the sludge may increase M-type hexaferrite formation temperature owing to barium or calcium sulfate formation in the precursor. The impurities also contribute to the difference in the microstructure for lower melting point. Possible applications of the sludge-derived hexaferrite products such as magnetic material or microwave absorber are suggested.

Keywords: Waste valorization; Sludge; Acid mine drainage; M-type hexaferrite; Solid-state reaction

1. Introduction

Acid mine drainage is one of the major pollutants of the mining industry. This generation of acidity can be continuous even when a mine has been abandoned for hundreds of years. Lime neutralization and its enhanced processes are the most widely

used methods to treat acid mine drainage (Zinck and Griffith, 2013). As a result, large amounts of metal-rich hydroxide sludge are produced during the treatment process (Macías et al., 2017). In addition to land occupation, the high disposal cost, and risk of toxic metal migration from sludge to land associated with sludge disposal at mine sites necessitate novel techniques for sludge recycling (Rakotonimaro et al., 2017).

Since it was discovered in the 1950s, M-type barium hexaferrite $BaFe_{12}O_{19}$ and its substituted or doped materials have been widely used in magnets, microwave devices, magnetic recording media, microwave absorbers, gas sensors, adsorbent, and so forth (Went, et al., 1952; Sixtus, et al., 1956; Harris, et al., 2009; Sözeri, et al., 2014; Karmakar, et al., 2014; Patel, et al., 2012). Annual global production of M-type barium hexaferrite exceeds 300,000 tons, which constitutes half of the total production of magnetic materials (Pullar, 2012). $BaFe_{12}O_{19}$ exists in a hexagonal magnetoplumbite structure, which affords it excellent magnetic properties and chemical stability (Goldman, 2006). Other sufficiently large divalent metal ions, such as strontium and lead, can substitute barium ions without too much distortion of the structure (Kojima, 1982). Calcium belongs to the same group as barium and strontium, and it is cheaper and more abundant. Unfortunately, calcium ions are too small to maintain the magnetoplumbite structure of undoped $CaFe_{12}O_{19}$. Doping with a small amount of lanthanum ions is an effective method to improve the structural stability of $CaFe_{12}O_{19}$ (Ichinose and Kurihara, 1963; Lotgering and Huyberts, 1980). In addition, calcium-substituted M-type barium and strontium hexaferrite have been successfully prepared (Blanco and Gonzalez, 1991; Iqbal, et al., 2010; Sanghi and Agarwal, 2012; Anbarasu, et al., 2013).

As summarized in the authors' review (Liu, et al., 2018), previous studies on waste-derived ferrite have mainly focused on using metal-rich wastes to fabricate spinel ferrites. Whereas studies of waste-derived hexaferrite, which has a wider range of applications and greater market share than spinel ferrite, are relatively rare. Pullar and co-workers were the first to use iron-rich sludge produced by a steel/iron-based wiredrawing process to synthesize undoped $SrFe_{12}O_{19}$ and Co/Mn-doped $SrCo_{0.5}Mn_{0.5}Fe_{11}O_{19}$ and $SrCoMnFe_{10}O_{19}$ with addition of $SrCO_3$, Co_3O_4, and $MnCl_2{\cdot}4H_2O$ (Pullar, et al., 2013). They subsequently used the same sludge to prepare undoped $BaFe_{12}O_{19}$ with addition of $BaCO_3$ (Pullar, et al., 2016). In both studies, the sludge was recycled and used only as the iron source in hexaferrite processing. And the reactions and mechanism of ferrite derived from wastes have not been sufficiently investigated.

In this study, acid mine drainage sludge was recycled as both alternative iron and calcium sources to synthesize M-type hexaferrite powders by solid-state reaction with addition of $BaCO_3$. Mixtures with initial compositions of $Ca_xBa_{1-x}Fe_{12}O_{19}$ (x = 0, 0.3, 0.5, 0.7, and 1.0) were prepared from different combinations of two types of acid mine drainage sludge (A and B), α-Fe_2O_3, and $BaCO_3$. The effect of sludge addition on phase formation and microstructure evolution during calcination was investigated, with special focus on the chemical reactions and mechanism of hexaferrite preparation from sludge. The crystalline M-type hexaferrite phase can be identified by XRD in as-prepared samples with addition of up to 93.9% (mass%) acid mine drainage sludge. Value-added products derived from the sludge and reduction of sludge accumulation in deposits at mine sites can therefore be expected.

2. Materials and methods

2.1. Materials

Two types of dewatered acid mine drainage sludge (A and B) were sampled from different sludge deposits of acid mine drainage treatment plants in Japan. Sludge A has higher calcium content than sludge B and was generated during a prevalent calcium carbonate and lime two-step neutralization process, whereas sludge B was generated during a less common bacterial oxidation and calcium carbonate neutralization process. The two types of sludge were dried in an oven at 105 °C for 24 h and their main elemental compositions (see Figure 1.) were determined by inductively coupled plasma atomic emission spectroscopy (ICP-AES) (Spectro Arcos, Ametek, Berwyn, PA, USA) after acid digestion by a $HCl–HNO_3–HF–H_3BO_3$ acid system. Figure S1 and S2 show the XRD patterns, micrographs and TG-MS curves of Sludge A and Sludge B, respectively. Both sludge flocs agglomerated to a few microns in length. Sludge A was characterized as amorphous iron hydroxide with excess neutralizer $Mg_{0.064}Ca_{0.936}CO_3$, whereas Sludge B mainly consisted of goethite (α-FeOOH) and ferric sulfate. α-Fe_2O_3 and $BaCO_3$ (99.9% purity, Wako Pure Chemical Industries, Ltd., Osaka, Japan) were used to adjust the initial molar ratio of Ca:Ba:Fe for the $Ca_xBa_{1-x}Fe_{12}O_{19}$ mixtures used in M-type hexaferrite preparation.

Figure 1. Main elemental compositions of the acid mine drainage sludge determined by ICP-AES (mass %): (a) sludge A and (b) sludge B.

2.2. Preparation of M-type hexaferrite

In previous studies, the impurities of wastes as alternative raw materials in ferrite production were purified by several processes (Liu, et al., 2018). However, these purification processes inevitably increase costs and consequently diminish the practicality of using wastes to prepare ferrite compounds. Considering the economic feasibility, the authors decided to completely reuse the acid mine drainage sludge without a preliminary purification process. The synthesis reaction of $Ca_xBa_{1-x}Fe_{12}O_{19}$ hexaferrite is represented by reaction (1).

$$x\text{CaO} + (1\text{-}x)\text{BaO} + 6\text{Fe}_2\text{O}_3 \rightarrow \text{Ca}_x\text{Ba}_{1-x}\text{Fe}_{12}\text{O}_{19} \quad (1)$$

Mixtures of the sludge and pure chemicals (see Table 1) with Ca:Ba:Fe = x:(1−x):12 (molar ratio) were wet ball-milled (Pulverisette 6, Fritsch GmbH, Idar-Oberstein, Germany) for 30 min, followed by drying at 105 °C for 24 h. The dried mixtures were then crushed and homogenized by mortar grinding to obtain the precursors, which were subsequently calcined in an alumina crucible at the target temperature with a holding time of 4 h using a box furnace without atmospheric control (KBF524N1, Koyo Thermo System Co., Ltd., Nara, Japan). Finally, the calcined samples were air-cooled in the furnace and ground into a powder in a mortar for analysis. The sludge-free mixture A_0F composed of α-Fe_2O_3 and $BaCO_3$ is used as a reference.

Table 1. Ingredient compositions of the $Ca_xBa_{1-x}Fe_{12}O_{19}$ (mass %) mixtures

Mixture	x	Sludge A	Sludge B	α-Fe_2O_3	$BaCO_3$
A_0F	0.0	0	0	82.9	17.1
A_1F	0.3	19.1	0	69.4	11.5
A_2F	0.5	31.1	0	61.0	7.9

A_3F	0.7	42.3	0	53.0	4.7
A_4F	1.0	57.8	0	42.1	0
A_0B	0.04	0	88.0	0	12.0
A_1B	0.3	12.3	79.2	0	8.5
A_2B	0.5	22.0	71.9	0	6.1
A_3B	0.7	31.7	64.6	0	3.7
A_4B	1.0	46.5	53.5	0	0

2.3. Characterization

2.3.1. Phase identification

The X-ray diffraction (XRD) patterns of the precursors and calcined samples were recorded by a Bruker D2 Phaser diffractometer with Cu-Kα radiation at 30 kV and 10 mA using a LYNXEYE detector (Bruker AXS GmbH, Karlsruhe, Germany). The 2θ scan range was 10°–80° with a step size of 0.02° and a scan speed of 0.5 s per step. Phase identification was performed by matching the XRD patterns of the samples to standard patterns retrieved from the database of the International Centre for Diffraction Data (ICDD, PDF 2010).

2.3.2. Morphological study

The morphologies of the calcined samples were determined by field-emission scanning electron microscopy (FE-SEM, SU6600, Hitachi High-Technologies Corporation, Tokyo, Japan).

2.3.3. Thermal analysis

The thermogravimetric and differential thermogravimetric (TG–DTG) curves of the precursors were recorded from room temperature to 1300 °C at a heating rate of 10 °C/min under a simulated air atmosphere (20% O_2–80% He) using a STA449F1 Jupiter simultaneous thermal analyzer (NETZSCH-Gerätebau GmbH, Wittelsbacherstraße, Germany) by NETZSCH Japan K.K, coupled with a JMS-Q1500GC mass spectrometer (JEOL Ltd., Tokyo, Japan) to analyze the evolved gas.

3. Results and discussion

3.1. Effect of sludge addition on phase formation during calcination

The crystalline phases in the precursors and samples prepared from sludge free A_0F and sludge added mixtures (see Table 1.) are summarized in Table 2. The XRD patterns are shown in Figures S3–S12. The results for the precursors indicate that the iron species in sludge A are quite different from those in sludge B. Crystalline iron oxyhydroxide (goethite, α-FeOOH, PDF 01-076-7156) can be identified only in the precursors containing sludge B. The iron in sludge A exists in an amorphous form, whereas residual crystalline $CaCO_3$ neutralizer is contained in the precursors not containing sludge B. Calcium or barium carbonate in the ingredients transforms to the sulfate with sludge B addition. High sulfur content in sludge B is believed to be responsible for this phenomenon.

Table 2. Changes in the crystalline phases observed during calcination.

Mixture	Crystalline phases observed					
	Precursor	900 °C/4 h	1000 °C/4 h	1100 °C/4 h	1200 °C/4 h	1300 °C/4 h

A_0F	α-Fe_2O_3; $BaCO_3$	**M-type hexaferrite**; α-Fe_2O_3	**M-type hexaferrite**; α-Fe_2O_3	**M-type hexaferrite**; α-Fe_2O_3	**M-type hexaferrite**; α-Fe_2O_3	**M-type hexaferrite**; α-Fe_2O_3
A_1F	α-Fe_2O_3; $BaCO_3$	**M-type hexaferrite**; α-Fe_2O_3; hexacelsian	**M-type hexaferrite**; α-Fe_2O_3; hexacelsian	**M-type hexaferrite**; α-Fe_2O_3	**M-type hexaferrite**; α-Fe_2O_3	**M-type hexaferrite**; α-Fe_2O_3; hexacelsian
A_2F	α-Fe_2O_3; $BaCO_3$; $CaCO_3$	α-Fe_2O_3; **M-type hexaferrite**; hexacelsian	α-Fe_2O_3; **M-type hexaferrite**; hexacelsian	α-Fe_2O_3; **M-type hexaferrite**;	α-Fe_2O_3; **M-type hexaferrite**;	α-Fe_2O_3; **M-type hexaferrite**;
A_3F	α-Fe_2O_3; $CaCO_3$	α-Fe_2O_3; hexacelsian	α-Fe_2O_3; hexacelsian	α-Fe_2O_3; **M-type hexaferrite**; hedenbergite aluminian	α-Fe_2O_3; **M-type hexaferrite**; hedenbergite aluminian; hexacelsian	α-Fe_2O_3; **M-type hexaferrite**; hedenbergite aluminian
A_4F	α-Fe_2O_3; $CaCO_3$	α-Fe_2O_3	α-Fe_2O_3; hedenbergite aluminian	α-Fe_2O_3; hedenbergite aluminian	α-Fe_2O_3; hedenbergite aluminian	α-Fe_2O_3
A_0B	α-FeOOH; $BaSO_4$; $BaCO_3$	α-Fe_2O_3; $BaSO_4$; hexacelsian	α-Fe_2O_3; $BaSO_4$; hexacelsian	**M-type hexaferrite**; α-Fe_2O_3; hexacelsian	**M-type hexaferrite**; α-Fe_2O_3; hexacelsian	**M-type hexaferrite**; α-Fe_2O_3; hexacelsian
A_1B	α-FeOOH; $BaSO_4$;	α-Fe_2O_3; $BaSO_4$;	α-Fe_2O_3; $BaSO_4$;	α-Fe_2O_3; **M-type**	α-Fe_2O_3; **M-type**	α-Fe_2O_3; **M-type**

	$BaCO_3$	hexacelsian	hexacelsian	**hexaferrite**; celsian	**hexaferrite**; celsian	**hexaferrite**; celsian
A_2B	α-FeOOH; $BaSO_4$; gypsum	α-Fe_2O_3; $BaSO_4$; hexacelsian; celsian	α-Fe_2O_3; $BaSO_4$; hexacelsian; celsian	α-Fe_2O_3; **M-type hexaferrite**; celsian	α-Fe_2O_3; **M-type hexaferrite**; celsian	α-Fe_2O_3; **M-type hexaferrite**; celsian
A_3B	α-FeOOH; gypsum; $BaSO_4$	α-Fe_2O_3; hexacelsian; celsian; $BaSO_4$	α-Fe_2O_3; hexacelsian; celsian;	α-Fe_2O_3; celsian;	α-Fe_2O_3; celsian;	α-Fe_2O_3; celsian; hexacelsian
A_4B	α-FeOOH; gypsum	α-Fe_2O_3; anorthite	α-Fe_2O_3; anorthite	α-Fe_2O_3; anorthite	α-Fe_2O_3; anorthite	α-Fe_2O_3; anorthite

It is worth noting that calcium-substituted and unsubstituted $BaFe_{12}O_{19}$ are difficult to distinguish by XRD because of their similar crystal structures (Anbarasu, et al., 2013). Therefore, the phase is labeled "M-type hexaferrite" rather than $BaFe_{12}O_{19}$ (PDF 00-043-0002). In the sludge-free A_0F series, the characteristic reflections of the (110), (107), (114), and (203) planes of M-type hexaferrite are observed in the XRD patterns of the samples calcined from 900 to 1300 °C. However, weak peaks corresponding to α-Fe_2O_3 (PDF 01-079-0007) are also present in the above temperature range.

Using sludge A as an alternative to α-Fe_2O_3 and $BaCO_3$ (series A_1F–A_4F), with increasing addition of sludge, there is an increase in the formation temperature and decreases in the intensities of the main peaks of M-type hexaferrite. In addition to the α-Fe_2O_3 phase, impurity phases, such as hexacelsian ($BaAl_2Si_2O_8$, PDF 01-072-7502) and hedenbergite aluminian ($Ca(Fe_{0.821}Al_{0.179})(SiAl_{0.822}Fe_{0.178}O_6)$, PDF 01-078-1546), are also present in the calcined samples. Because of the structural instability of undoped

$CaFe_{12}O_{19}$, it is not surprising that no M-type hexaferrite can be identified in the A_4F series without $BaCO_3$ addition over the whole temperature range.

Using both sludge A and sludge B as alternative materials (series A_0B–A_4B), the XRD patterns of the calcined samples are more complex compared with those of series A_0F–A_4F. The intensities of the main peaks of M-type hexaferrite for the calcined samples are weaker than those for the A_0F–A_4F samples under the same conditions. For low $BaCO_3$ addition (3.7 mass %) in the A_3B series and no $BaCO_3$ addition in the A_4B series, M-type hexaferrite cannot be identified. Another difference is that the peaks corresponding to M-type hexaferrite start to appear above 1100 °C, which is accompanied by the peaks corresponding to $BaSO_4$ disappearing. This suggests that M-type hexaferrite forms after decomposition of $BaSO_4$. Some of the hexacelsian impurity phase transforms to another barium aluminosilicate crystalline phase (celsian, $BaAl_2Si_2O_8$, PDF 00-038-1450). The results indicate that higher calcium content or higher temperature promotes this phase transformation. Hedenbergite aluminian is not observed for these series, and anorthite ($CaAl_2Si_2O_8$, PDF 01-075-1587) is present in the A_4B series.

For M-type hexaferrite production, it is clear that the iron source α-Fe_2O_3 can be completely replaced by acid mine drainage sludge. The iron in the sludge, regardless of whether it is in the form of crystalline iron oxyhydroxide, poorly crystalline ferrihydrite, or ferric sulfate, first transforms to the intermediate α-Fe_2O_3 phase and then participates in the reactions of hexaferrite production. In contrast, the other raw material $BaCO_3$ can only be partially replaced by the calcium in the sludge to form calcium-substituted M-type barium hexaferrite.

The presence of aluminum and silicon impurities in the acid mine drainage sludge leads to formation of barium or calcium aluminosilicates in the calcined samples. Sulfur (another impurity in the sludge) may increase the temperature when M-type hexaferrite starts to form owing to barium or calcium sulfate formation in the precursor.

3.2. Effect of sludge addition on microstructure evolution

Using acid mine drainage sludge as an alternative raw material in M-type hexaferrite preparation also affects the microstructure of the calcined sample. Figure 2. shows a comparison of the FE-SEM micrographs of samples with and without sludge addition calcined at 900–1300 °C for 4 h. The sludge-free A_0F series exhibit plate-like shaped grains of M-type hexaferrite with random orientations. The grains grow larger and thicker with increasing calcination temperature. In the case of the A_0B series, bulk α-Fe_2O_3 is covered by irregularly shaped particles at 900 and 1000 °C. The sintering phenomenon is observed above 1200 °C, and the particles grow as spiral hillocks with small steps. The impurities in the sludge are believed to lower the melting point, which results in a different crystal growth model from the sludge-free samples (Elwell and Neate, 1971; Vinnik, et al., 2017).

Figure 2. Comparison of the micrographs of A_0F and A_0B calcined at 900–1300 °C for 4 h.

3.3. Proposed reactions and mechanism

Figure 3. shows the TG–DTG curves of precursors A_0F, A_0B, A_2B, and A_4B, respectively. The m/z = 18 (H_2O^+), 44 (CO_2^+), and 64 (SO_2^+) ion current curves of the

above four precursors are shown in Figure 4. Significant differences are observed in the decomposition processes of the precursors with different addition of acid mine drainage sludge.

Figure 3. TG–DTG curves of the representative precursors: (a) A_0F, (b) A_0B, (c) A_2B, and (d) A_4B.

Figure 4. Effect of sludge addition on gas evolution during heating under a simulated air atmosphere (20% O_2 and 80% He): (a) m/z = 18 (H_2O^+), (b) m/z = 44 (CO_2^+), and (c) m/z = 64 (SO_2^+).

As shown in Table 1, the A_0F precursor is a mixture of the pure chemicals α-Fe_2O_3 and $BaCO_3$, and it exhibits two DTG peaks at 294 and 757 °C (Figure 3(a)). From the MS curves, the former peak corresponds to mass loss of water, whereas the latter peak corresponds to decomposition of $BaCO_3$ (eq 2).

$$BaCO_3 \rightarrow BaO + CO_2 \quad (2)$$

Another contribution to CO_2 evolution in the range 200–400 °C is decomposition of carbonaceous matter. The peak at 1079 °C in the m/z = 64 ion current curve of the A_0F precursor can be attributed to release of trace SO_2. The possible sources of carbonaceous matter and trace sulfate are water added during the wet ball milling process and trace impurities in the pure chemicals.

With replacement of α-Fe_2O_3 by sludge B (A_0B precursor), three DTG peaks and larger mass loss are observed (Figure 3(b)). Both dehydration and dehydroxylation reactions are considered to be responsible for the mass loss of water of the A_0B

precursor (Alcolea, et al., 2010). The probable reactions are represented by reaction (3), (4) and (5).

$Fe_2(SO_4)_3 \cdot xH_2O \rightarrow Fe_2(SO_4)_3 + xH_2O$ (3)

$2Fe(OH)_3 \rightarrow Fe_2O_3 + 3H_2O$ (4)

$2Al(OH)_3 \rightarrow Al_2O_3 + 3H_2O$ (5)

Compared with the A_0F precursor, there is a marked decrease in mass loss corresponding to carbonate decomposition and an increase in mass loss ascribed to carbonaceous matter decomposition for the A_0B precursor. The latter is believed to be a result of flocculants added in the acid mine drainage treatment process. Combined with a clear increase in SO_2^+ evolution, the former can be attributed to $BaCO_3$ transforming to $BaSO_4$ during the mixing process with sludge B addition. The peak at 620 °C in the DTG curve of the A_0B precursor is believed to be transformation of $Fe_2(SO_4)_3$ to Fe_2O_3, and the peak at 1136 °C corresponds to decomposition of $BaSO_4$. The desulfation reactions to be considered are represented by reaction (6) and (7).

$Fe_2(SO_4)_3 \rightarrow Fe_2O_3 + 3SO_2 + 3/2O_2$ (6)

$BaSO_4 \rightarrow BaO + SO_2 + 1/2O_2$ (7)

For the A_2B and A_4B precursors (Figure 3(c) and (d)), the total mass loss is almost the same as that of the A_0B precursor. However, the mass loss steps and gas evolution are different owing to the different proportions of sludge A, sludge B, and $BaCO_3$. As previously mentioned, sludge A and sludge B are generated by different acid mine drainage treatment processes, which results in the two types of sludge having different compositions. A possible reason for the discrepancy in water evolution at around 110 °C between A_4B and the other three precursors might be the abundance of poorly

crystalline ferrihydrite-like $Fe_5O_7(OH)\cdot 4H_2O$ in the A_4B precursor (Pulišová, et al., 2014). The DTG peak at 109 °C may correspond to the loss of water during the transformation of ferrihydrite to goethite (eq 8), and the peak at 244 °C corresponds to dehydroxylation of goethite (eq 9):

$$Fe_5O_7(OH)\cdot 4H_2O \rightarrow 5FeOOH + 2H_2O \quad (8)$$

$$2FeOOH \rightarrow Fe_2O_3 + H_2O \quad (9)$$

The peaks corresponding to carbonate decomposition are completely absent in the curves of the A_2B and A_4B precursors. For SO_2 evolution, the peaks at around 1000 °C are considered to be because of $CaSO_4$ decomposition (eq 10):

$$CaSO_4 \rightarrow CaO + SO_2 + 1/2O_2 \quad (10)$$

The variation in SO_2^+ evolution corresponding to $CaSO_4$ and $BaSO_4$ decomposition among the A_0B, A_2B, and A_4B precursors depends on the amounts of sludge A, sludge B, and $BaCO_3$.

A combined XRD and TG–MS study shows that the chemical composition and mineral composition of acid mine drainage sludge have a considerable effect on the reaction pathways and final calcination products. The proposed reaction pathways of (a) the sludge-free sample (A_0F), (b) only sludge A as an alternative raw material (A_1F–A_4F), and (c) both sludge A and sludge B as alternative raw materials (A_0B–A_4B) are shown in Figure 5. The α-Fe_2O_3 intermediate forms by dehydroxylation or desulfation reactions in sludge addition pathways (b) and (c). In particular, for addition of sludge B with relatively high sulfur content, a barium sulfate or calcium sulfate intermediate forms during the wet ball-milling process, which results in an increase in the preparation temperature of M-type hexaferrite. Impurities such as Al and Si are common in acid mine drainage sludge. There is competition between the CaO–BaO–Fe_2O_3 and CaO–

$BaO–Al_2O_3–SiO_2$ systems, which would have a negative effect on the efficiency of Ca and Ba in M-type hexaferrite preparation.

Figure 5. Proposed reaction pathways of M-type hexaferrite preparation: (a) sludge free, (b) sludge A, and (c) both sludge A and sludge B.

3.4 Possible applications of the acid mine drainage sludge-derived hexaferrite

The pure M-type hexaferrite has a wide range of applications as we mentioned before. In the case of the sludge- derived hexaferrite, the effect of secondary phases need to be considered.

For applications as a magnetic material, the nonmagnetic secondary phases have negative effects on performance. Separation of magnetic phases from nonmagnetic phases might enhances the performance of the sludge-derived products. But it is evidently a big challenge for practice. And the residues after separation have to be considered.

For application in microwave absorber, the secondary phases are not always detrimental. For example, celsian also contributes to microwave absorption (Li, et al., 2016). Therefore the acid mine drainage sludge-derived hexaferrite products have potential to use without further purification process after calcination.

Furthermore, future work will deal with optimization of the amount of sludge addition for hexaferrite synthesis in microwave absorption and other applications.

4. Conclusion

The present study indicates that acid mine drainage sludge can be completely reused to produce value-added M-type hexaferrite by a solid-state reaction process. It is expected that reduction in sludge accumulation in deposits at mine sites using this process. The findings suggest how the impurities in the sludge, such as silicon, aluminum, and sulfur, are involved in phase formation and microstructure evolution of the calcined samples. A fundamental understanding of the behavior of metal-rich sludge in M-type hexaferrite preparation can be achieved. In addition, possible applications of M-type hexaferrite prepared from acid mine drainage sludge as a microwave absorber or magnetic material are proposed. The magnetic properties and microwave absorption properties of the as-prepared products will be investigated in future work.

Acknowledgments

We gratefully acknowledge financial support from the Management Expenses Grants for National Universities Corporations "Dynamic Alliance for Open Innovation Bridging Human, Environment and Materials" from the Ministry of Education, Culture, Sports, Science and Technology (MEXT) of Japan, and the Hatakeyama Culture Foundation. Mei Liu also acknowledges support from the Japanese government (MEXT) for a doctoral scholarship. Part of this research was performed as joint research with the Metals Environmental Management Department, Japan Oil, Gas and Metals National Corporation (JOGMEC), and we would like to express our thanks to them for valuable technical discussions and support in sludge sampling. We also thank the Fundamental Technology Center, Research Institute of Electrical Communication, Tohoku University for the FE-SEM observations performed with a Hitachi SU6600

scanning electron microscope. We thank Edanz Group (www.edanzediting.com/ac) for editing a draft of this manuscript.

Appendix A. Supplementary data

References

Alcolea, A., Ibarra, I., Caparrós, A., Rodríguez, R. **Study of the MS response by TG–MS in an acid mine drainage efflorescence.** J. Therm. Anal. Calorim. 101 (2010), pp. 1161–1165. https://doi:10.1007/s10973-009-0556-8.

Anbarasu, V., Md Gazzali, P.M., Karthik, T., Manigandan, A., Sivakumar, K. **Effect of divalent cation substitution in the magnetoplumbite structured $BaFe_{12}O_{19}$ system.** J. Mater. Sci. Mater. Electron. 24 (2013), pp. 916–926. https://doi:10.1007/s10854-012-0850-2.

Blanco, A.M., Gonzalez, F.C. **Magnetic properties and distribution of Ca ions in Ca-substituted Ba-ferrite.** J. Phys. D: Appl. Phys. 24 (1991), pp. 612–618. https://doi.org/10.1088/0022-3727/24/4/013.

Elwell, D., Neate, B.W. **Mechanisms of crystal growth from fluxed melts.** J. Mater. Sci. 6 (1971), pp. 1499–1519. https://doi:10.1007/BF02403090.

Goldman, **A. Modern Ferrite Technology, 2nd ed.** Springer Science and Business Media, Inc., Pittsburgh (2006).

Harris, V.G., Geiler, A., Chen, Y., Yoon, S.D., Wu, M., Yang, A., Chen, Z., He, P., Parimi, P. V., Zuo, X., Patton, C.E., Abe, M., Acher, O., Vittoria, C. **Recent advances in processing and applications of microwave ferrites.** J. Magn. Magn. Mater. 321 (2009), pp. 2035–2047. https://doi:10.1016/J.JMMM.2009.01.004.

Ichinose, N., Kurihara, K. A new ferrimagnetic compound. J. Phys. Soc. Japan 18 (1963), pp. 1700–1701. https://doi:10.1143/JPSJ.18.1700.

Iqbal, M.J., Ashiq, M.N., Hussain, I.H. **Physical, electrical and dielectric properties of Ca-substituted strontium hexaferrite ($SrFe_{12}O_{19}$) nanoparticles synthesized by co-precipitation method.** J. Magn. Magn. Mater. 322 (2010), pp. 1720–1726. https://doi.org/10.1016/j.jmmm.2009.12.013.

Karmakar, M., Mondal, B., Pal, M., Mukherjee, K. **Acetone and ethanol sensing of barium hexaferrite particles: A case study considering the possibilities of non-**

conventional hexaferrite sensor. Sensors Actuators B Chem. 190 (2014), pp. 627–633. https://doi:10.1016/J.SNB.2013.09.035.

Kojima, H. **Fundamental properties of hexagonal ferrites with magnetoplumbite structure, in: Wohlfarth, E.P. (Ed.), Ferromagnetic Materials.** North-Holland Publishing Company, New York (1982), pp. 305.

Li, M., Yin, X., Chen, L., Han, M., Cheng, L., Zhang, L. **Dielectric and electromagnetic wave absorption properties of reduced graphene oxide/barium aluminosilicate glass–ceramic composites.** Ceram. Int. 42 (2016), pp. 7099–7106. https://doi:10.1016/J.CERAMINT.2016.01.098.

Liu, M., Iizuka, A., Shibata, E. **Recent progress on utilization of metal-rich wastes in ferrite processing: a review.** Waste Biomass Valori. 9 (2018), pp. 1669-1679. https://doi.org/10.1007/s12649-017-9909-x.

Lotgering, F.K., Huyberts, M.A.H. **Composition and magnetic properties of hexagonal Ca, La ferrite with magnetoplumbite structure.** Solid State Commun. 34 (1980), pp. 49–50. https://doi:10.1016/0038-1098(80)90627-4.

Macías, F., Pérez-López, R., Caraballo, M.A., Cánovas, C.R., Nieto, J.M. **Management strategies and valorization for waste sludge from active treatment of extremely metal-polluted acid mine drainage: A contribution for sustainable mining.** J. Clean. Prod. 141 (2017), pp. 1057–1066. https://doi:10.1016/j.jclepro.2016.09.181.

Patel, H. A.; Byun, J.; Yavuz, C. T. **Arsenic removal by magnetic nanocrystalline barium hexaferrite.** J. Nanoparticle Res. 14 (2012), pp. 881. https://doi:10.1007/s11051-012-0881-x.

Pulišová, P., Máša, B., Michalková, E., Večerníková, E., Maříková, M., Bezdička, P., Murafa, N., Šubrt, J. **Thermal behaviour of natural and synthetic iron precipitates from mine drainage.** J. Therm. Anal. Calorim. 116 (2014), pp. 625–632. https://doi:10.1007/s10973-014-3759-6.

Pullar, R.C. Hexagonal ferrites: **A review of the synthesis, properties and applications of hexaferrite ceramics.** Prog. Mater. Sci. 57 (2012), pp. 1191–1334. https://doi:10.1016/J.PMATSCI.2012.04.001.

Pullar, R.C., Hajjaji, W., Amaral, J.S., Seabra, M.P., Labrincha, J. A. **Magnetic properties of ferrite ceramics made from wastes.** Waste Biomass Valori. 5 (2013), pp. 133–138. https://doi:10.1007/s12649-013-9207-1.

Pullar, R.C., Saeli, M., Novais, R.M., Amaral, J.S., Labrincha, J.A. **Valorisation of industrial iron oxide waste to produce magnetic barium hexaferrite.** Chem. Sel. 1 (2016), pp. 819–825. https://doi:10.1002/slct.201500042.

Rakotonimaro, T. V., Neculita, C. M., Bussière, B., Benzaazoua, M., Zagury, G. J. **Recovery and Reuse of Sludge from Active and Passive Treatment of Mine Drainage-Impacted Waters: A Review.** Environ. Sci. Pollut. Res. 24 (2017), pp. 73–91. https://doi.org/10.1007/s11356-016-7733-7.

Sanghi, S., Agarwal, A. **Rietveld refinement, electrical properties and magnetic characteristics of Ca–Sr substituted barium hexaferrites.** J. Alloys Compd. 513 (2012), pp. 436–444. https://doi.org/10.1016/j.jallcom.2011.10.071.

Sixtus, K.J., Kronenberg, K.J., Tenzer, R.K. **Investigations on barium ferrite magnets.** J. Appl. Phys. 27 (1956), pp. 1051–1057. https://doi:10.1063/1.1722540.

Sözeri, H., Deligöz, H., Kavas, H., Baykal, A. **Magnetic, dielectric and microwave properties of M–Ti substituted barium hexaferrites (M=Mn^{2+}, Co^{2+}, Cu^{2+}, Ni^{2+}, Zn^{2+}).** Ceram. Int. 40 (2014), pp. 8645–8657. https://doi:10.1016/J.CERAMINT.2014.01.082.

Vinnik, D., Tarasova, A., Zherebtsov, D., Gudkova, S., Galimov, D., Zhivulin, V., Trofimov, E., Nemrava, S., Perov, N., Isaenko, L., Niewa, R. **Magnetic and structural properties of barium hexaferrite $BaFe_{12}O_{19}$ from various growth techniques.** Materials (Basel) 10 (2017), pp. 578. https://doi:10.3390/ma10060578.

Went, J.J, Rathenau, G.W., Gorter, E.W., van Sterhout, G.W. **Ferroxdure, a class of new permanent magnet materials.** Philips Techn. Rev. 13(1952), pp. 194–208.

Zinck, J., Griffith, W. **Review of mine drainage treatment and sludge management operations.** MEND Report 3.43.1, Mining Association of Canada, Ottawa (2013). http://mend-nedem.org/wp-content/uploads/3.43.1_ReviewMineDrainageTreatmentSludge.pdf.

Figure

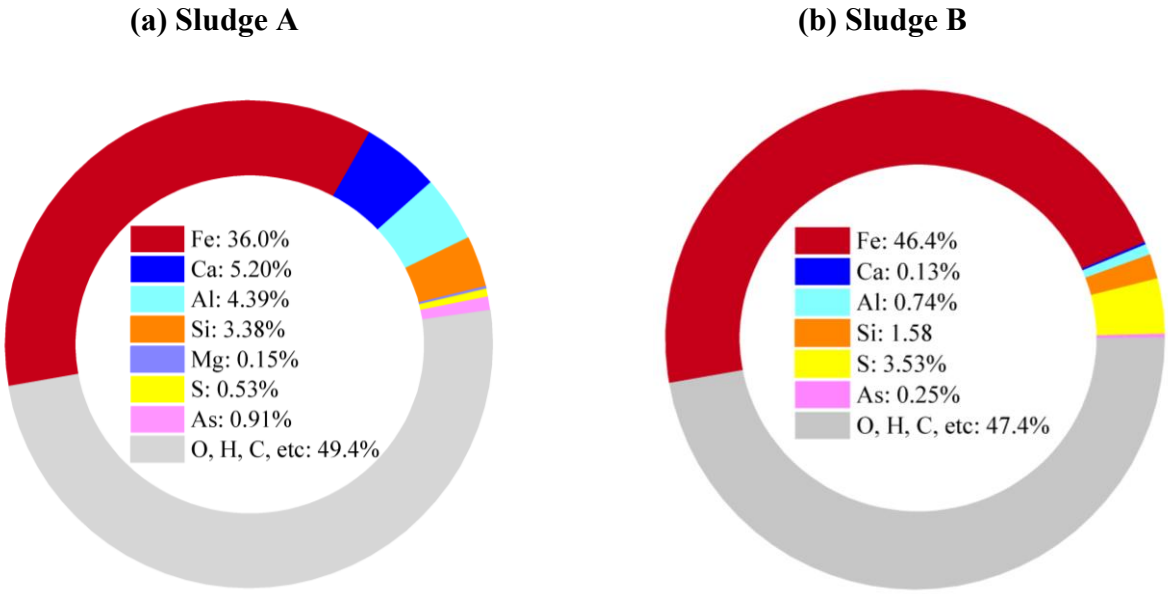

Fig. 1. Main elemental compositions of the acid mine drainage sludge determined by ICP-AES (mass %).

Figure

(a) A_0F-900 ºC

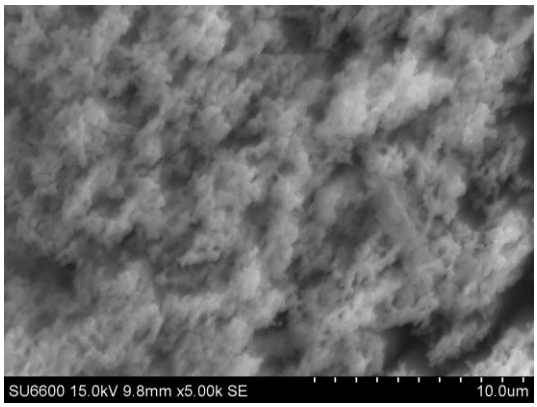

(b) A_0F-1000 ºC

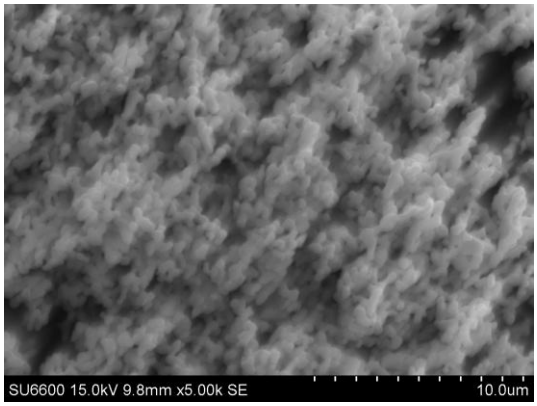

(c) A_0F-1100 ºC

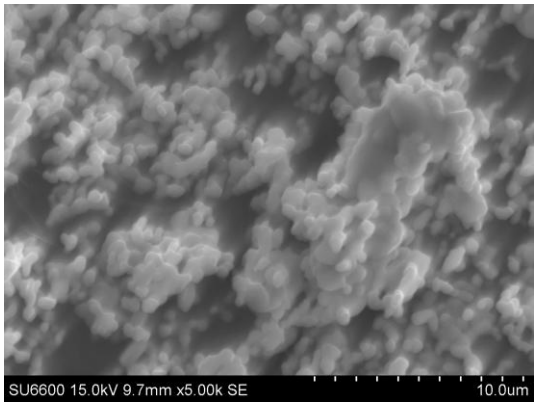

(d) A_0F-1200 ºC

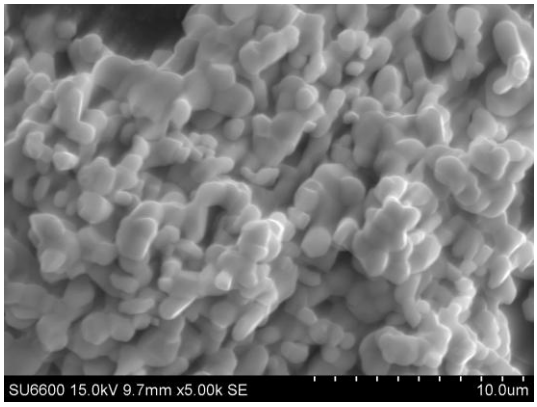

(f) A_0B-900 ºC

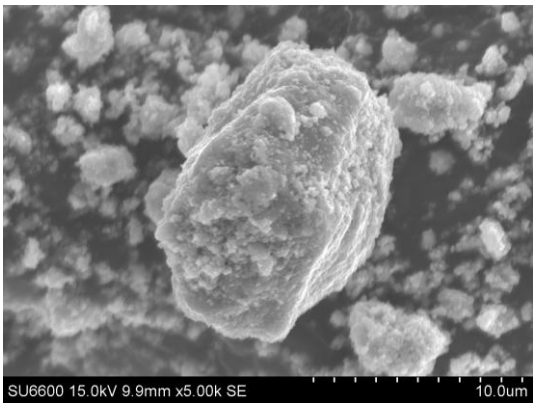

(g) A_0B-1000 ºC

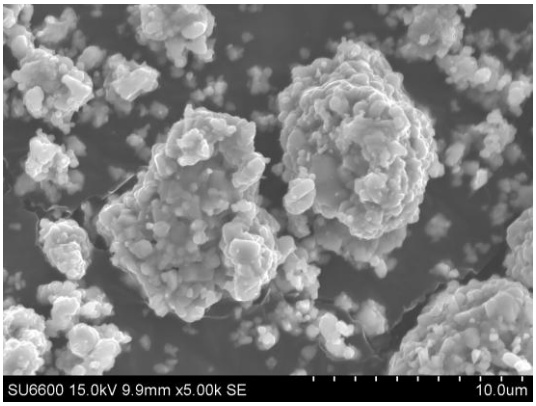

(h) A_0B-1100 ºC

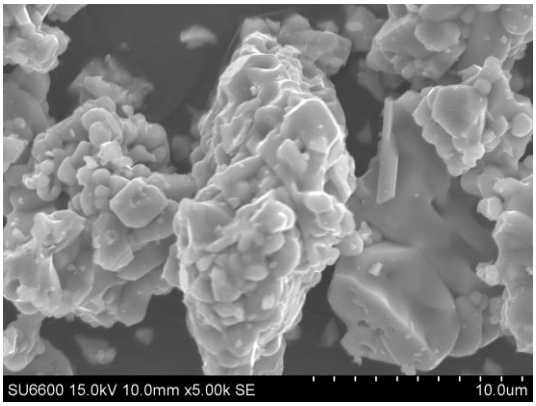

(i) A_0B-1200 ºC

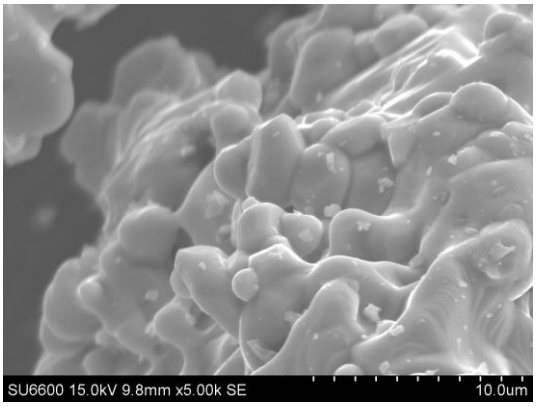

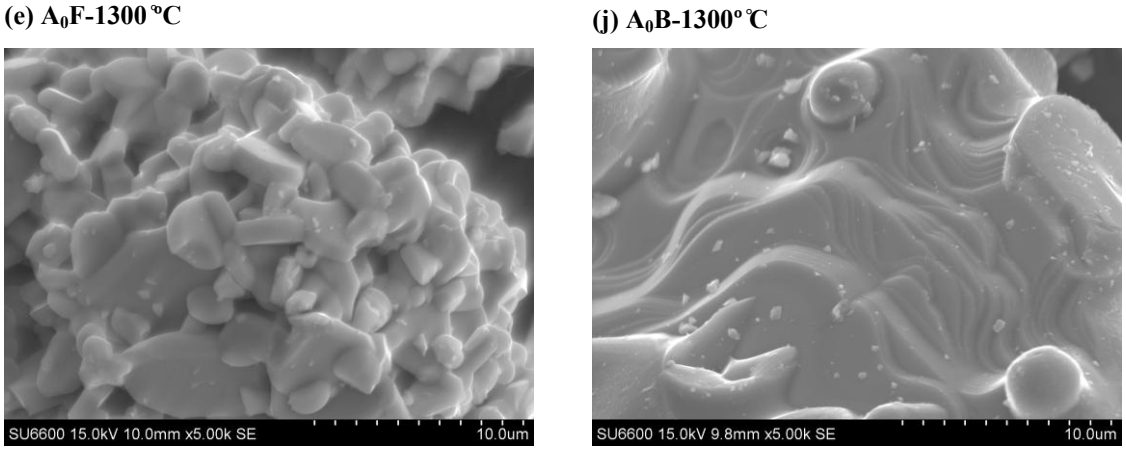

Fig. 2. Comparison of the micrographs of A_0F and A_0B calcined at 900–1300 °C for 4 h.

Figure

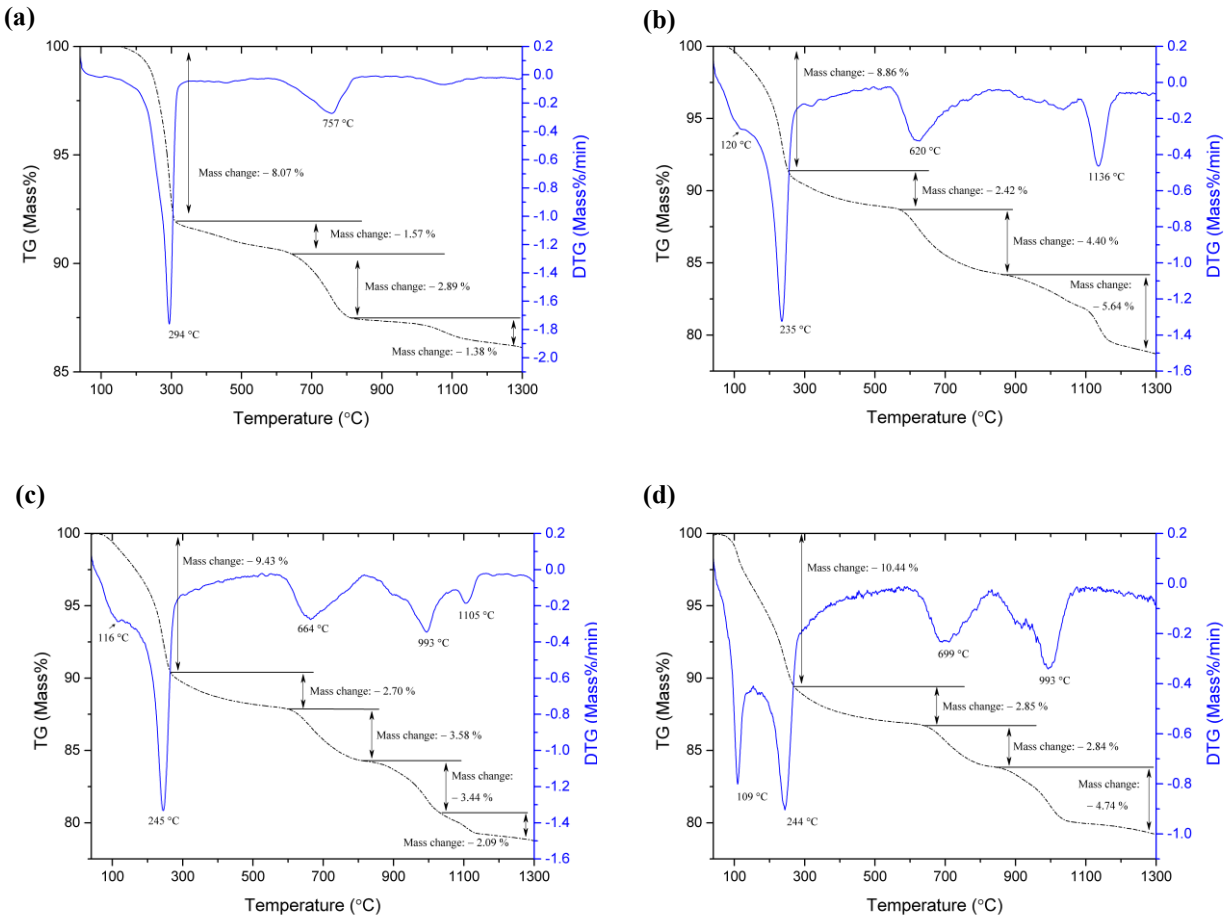

Fig. 3. TG–DTG curves of the representative precursors: (a) A_0F, (b) A_0B, (c) A_2B and (d) A_4B.

Figure

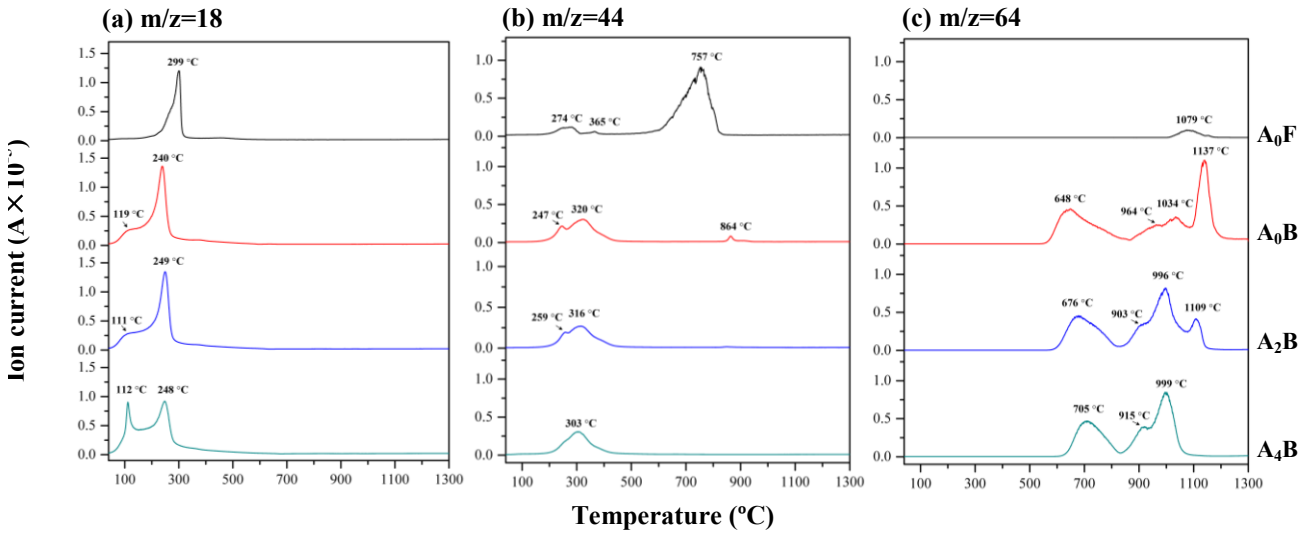

Fig. 4. Effect of sludge addition on gas evolution during heating under a simulated air atmosphere (20% O_2 and 80% He): (a) m/z = 18 (H_2O^+), (b) m/z = 44 (CO_2^+), and (c) m/z = 64 (SO_2^+).

Figure

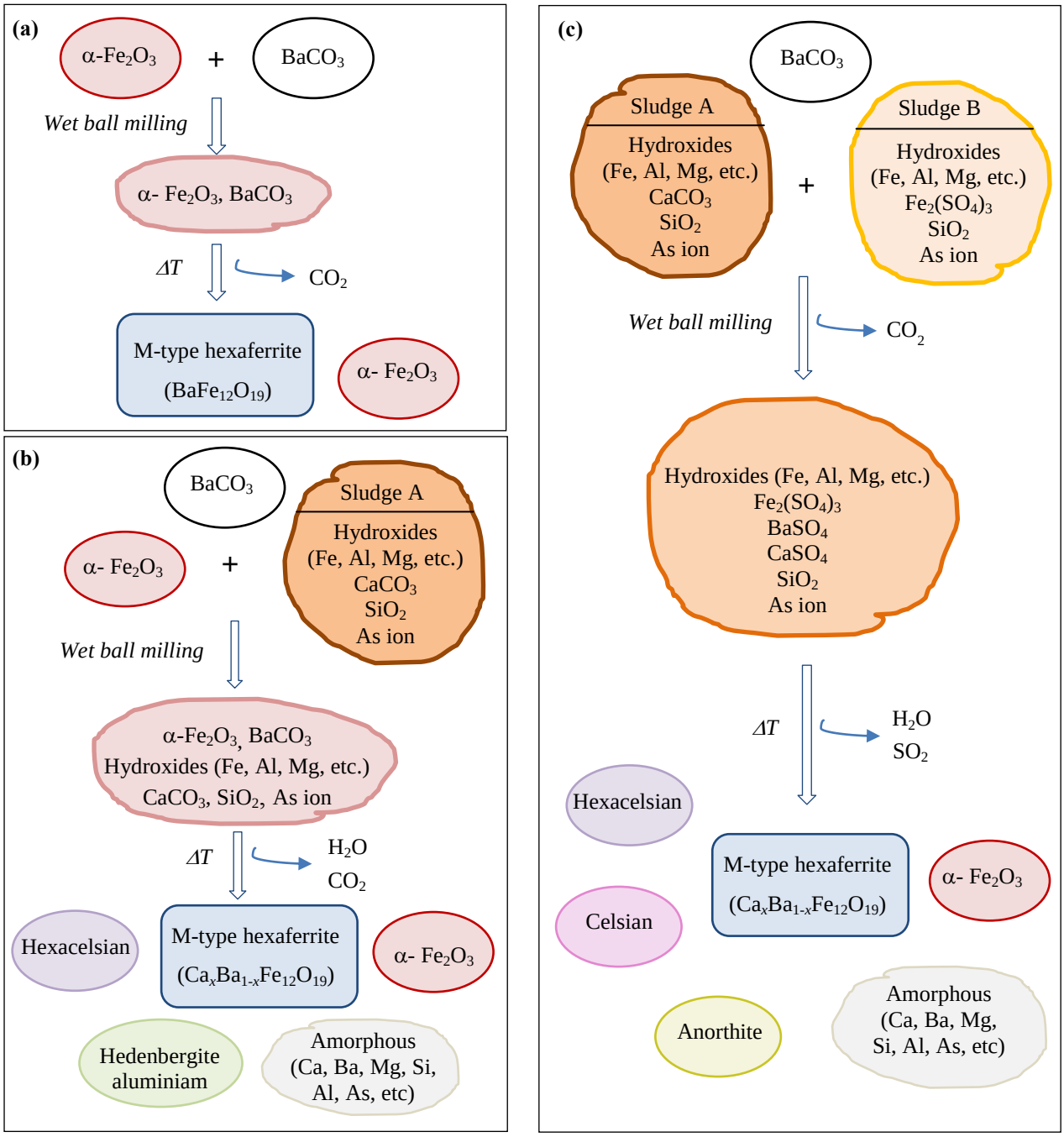
(a)
α-Fe2O3
+
BaCO3
Wet ball milling
α- Fe2O3, BaCO3
ΔT
CO2
M-type hexaferrite
(BaFe12O19)
α- Fe2O3
(b)
BaCO3
α- Fe2O3
+
Sludge A
Hydroxides
(Fe, Al, Mg, etc.)
CaCO3
SiO2
As ion
Wet ball milling
α-Fe2O3, BaCO3
Hydroxides (Fe, Al, Mg, etc.)
CaCO3, SiO2, As ion
ΔT
H2O
CO2
Hexacelsian
M-type hexaferrite
(CaxBa1-xFe12O19)
α- Fe2O3
Hedenbergite
aluminiam
Amorphous
(Ca, Ba, Mg, Si,
Al, As, etc)
(c)
BaCO3
Sludge A
Hydroxides
(Fe, Al, Mg, etc.)
CaCO3
SiO2
As ion
+
Sludge B
Hydroxides
(Fe, Al, Mg, etc.)
Fe2(SO4)3
SiO2
As ion
Wet ball milling
CO2
Hydroxides (Fe, Al, Mg, etc.)
Fe2(SO4)3
BaSO4
CaSO4
SiO2
As ion
ΔT
H2O
SO2
Hexacelsian
M-type hexaferrite
(CaxBa1-xFe12O19)
α- Fe2O3
Celsian
Anorthite
Amorphous
(Ca, Ba, Mg,
Si, Al, As, etc)

Graphical Abstract

Applications of M-type hexaferrite

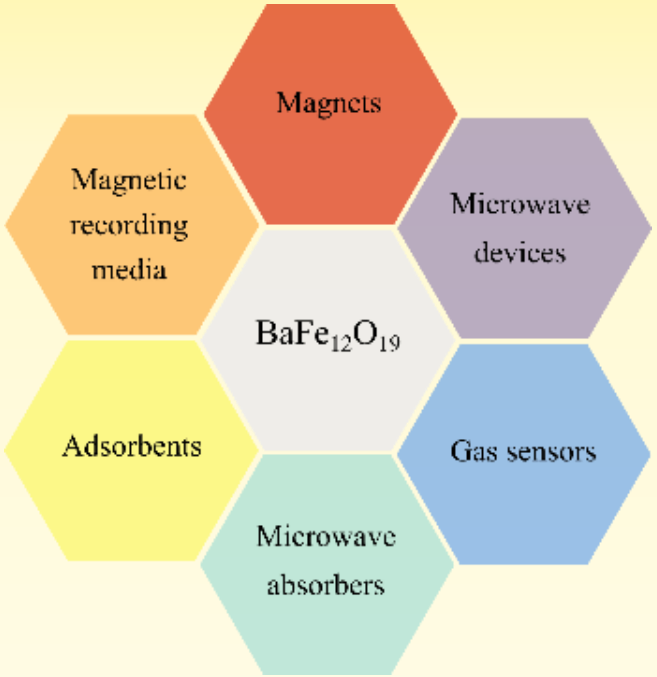

Reuse of AMD sludge in M-type hexaferrite preparation

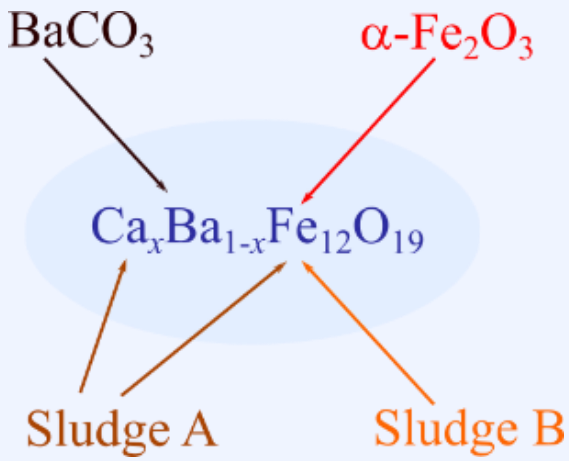

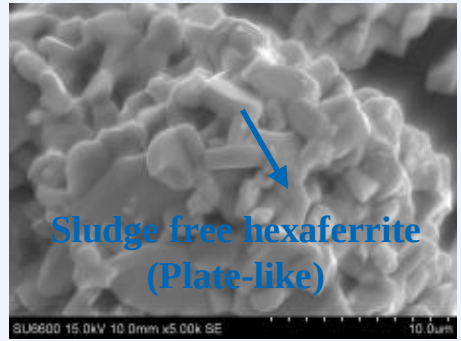

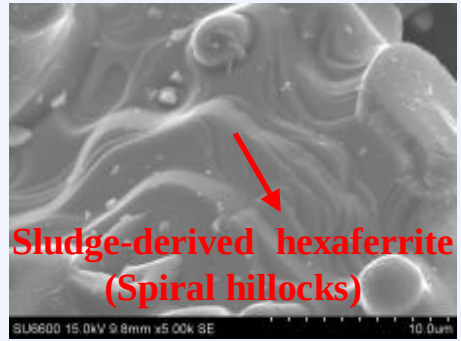

Supporting Information for

Acid Mine Drainage Sludge as an Alternative Raw Material for M-type Hexaferrite Preparation

Mei Liu [a, b, *], Atsushi Iizuka[c], Etsuro Shibata[c]

[a] Graduate School of Environmental Studies, Tohoku University, Sendai 980-0845, Japan

[b] School of Material Science and Engineering, Jingdezhen Ceramic Institute, Jingdezhen 333403, China

[c] Institute of Multidisciplinary Research for Advanced Materials (IMRAM), Tohoku University, Sendai 980-8577, Japan

*To whom correspondence should be addressed.

* M. Liu: liu.mei.q5@dc.tohoku.ac.jp; maggieliujci@gmail.com

Prof. A. Iizuka: atsushi.iizuka.e4@tohoku.ac.jp

Prof. E. Shibata: etsuro.shibata.e3@tohoku.ac.jp

Crystalline iron oxide or hydroxide was not identified from XRD patterns. Iron may exist as amorphous iron hydroxide.

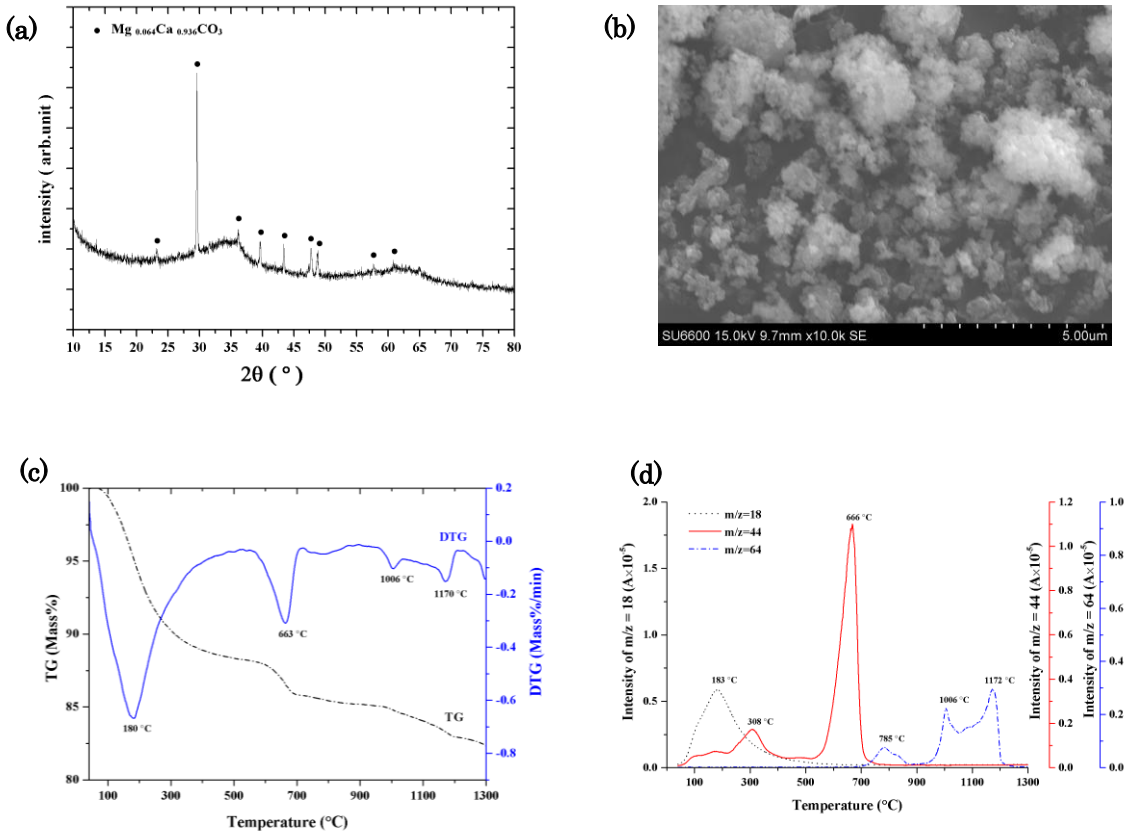

Figure S1. XRD patterns, micrograph, and TG-MS curves of dried Sludge A. (a) XRD; (b) micrograph; (c) TG-DTG curves; (d)MS curves. [1]

α-FeOOH was identified by XRD.

The TG-MS suggested that iron also existed as ferric sulfate.

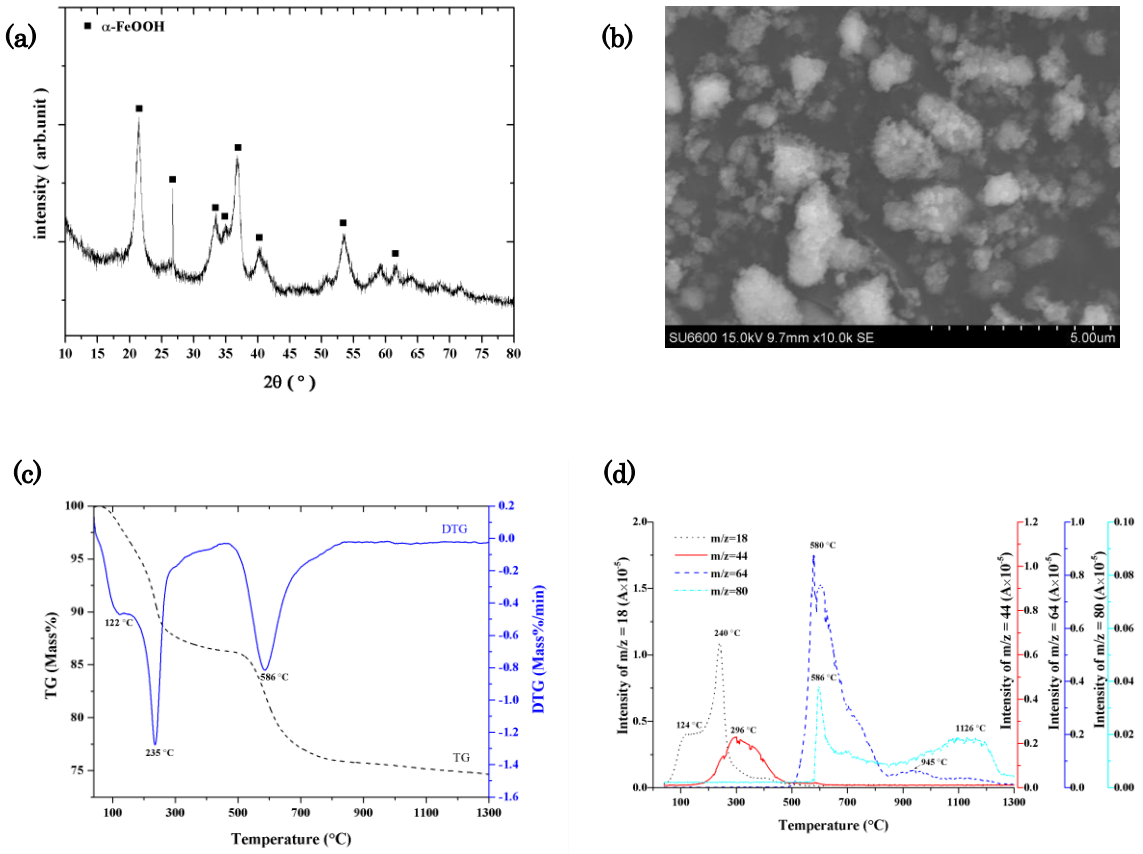

Figure S2. XRD patterns, micrograph, and TG-MS curves of dried Sludge B. (a) XRD; (b) micrograph; (c) TG-DTG curves; (d)MS curves. [1]

Ref.

[1] Liu, M., Iizuka, A., Shibata, E. **Effect of Temperature on Phase Transformation and Leaching Behavior of Acid Mine Drainage Sludge.** Mater. Trans. (in press) https://doi.org/10.2320/matertrans.M-M2018848

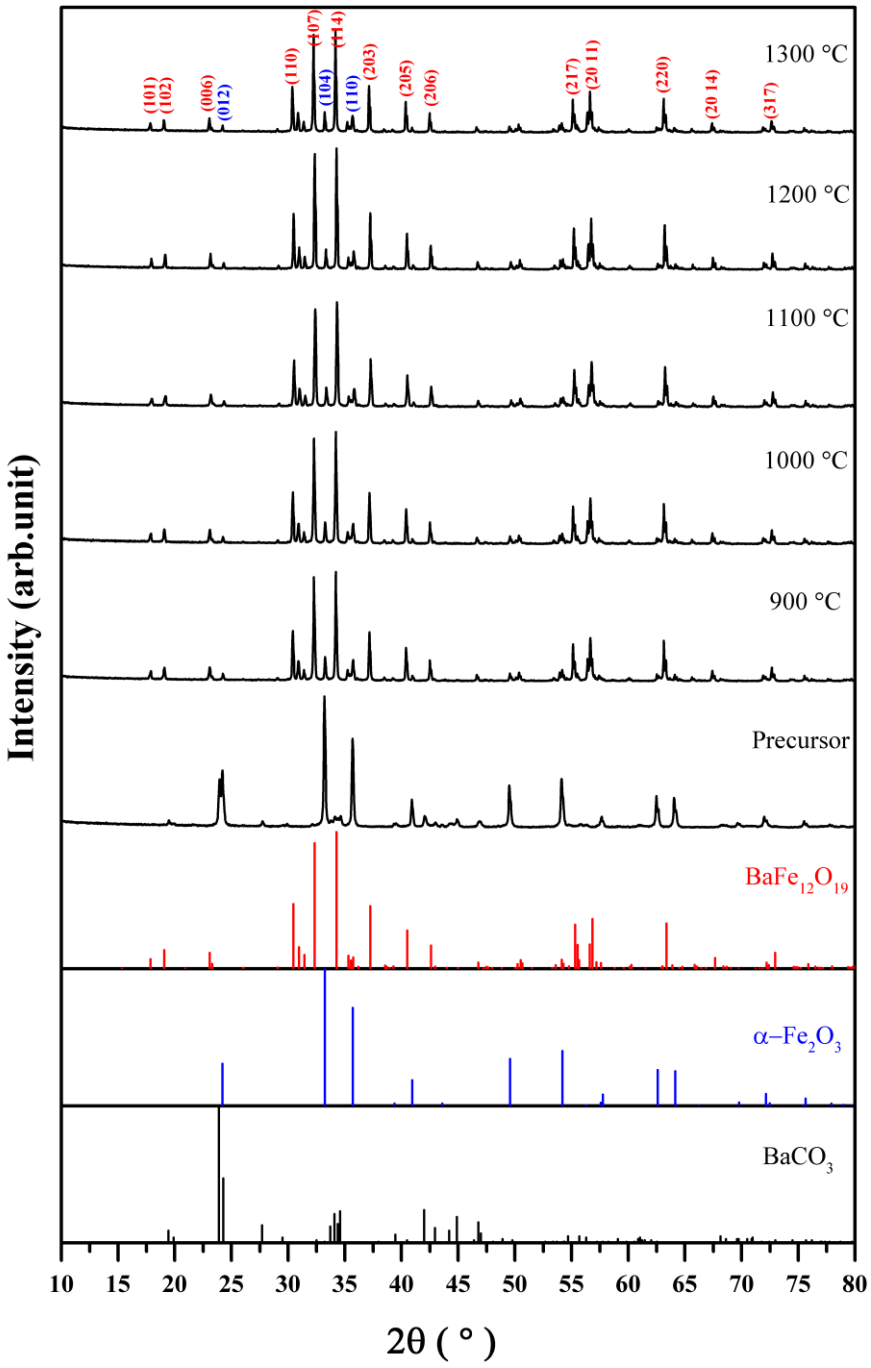

Figure S3. XRD patterns of A_0F before and after calcination at the target temperature for 4 h. The standard patterns retrieved from the database of the ICDD include $BaFe_{12}O_{19}$ (PDF 00-043-0002), α-Fe_2O_3 (PDF 01-079-0007), and $BaCO_3$ (PDF 00-044-1487).

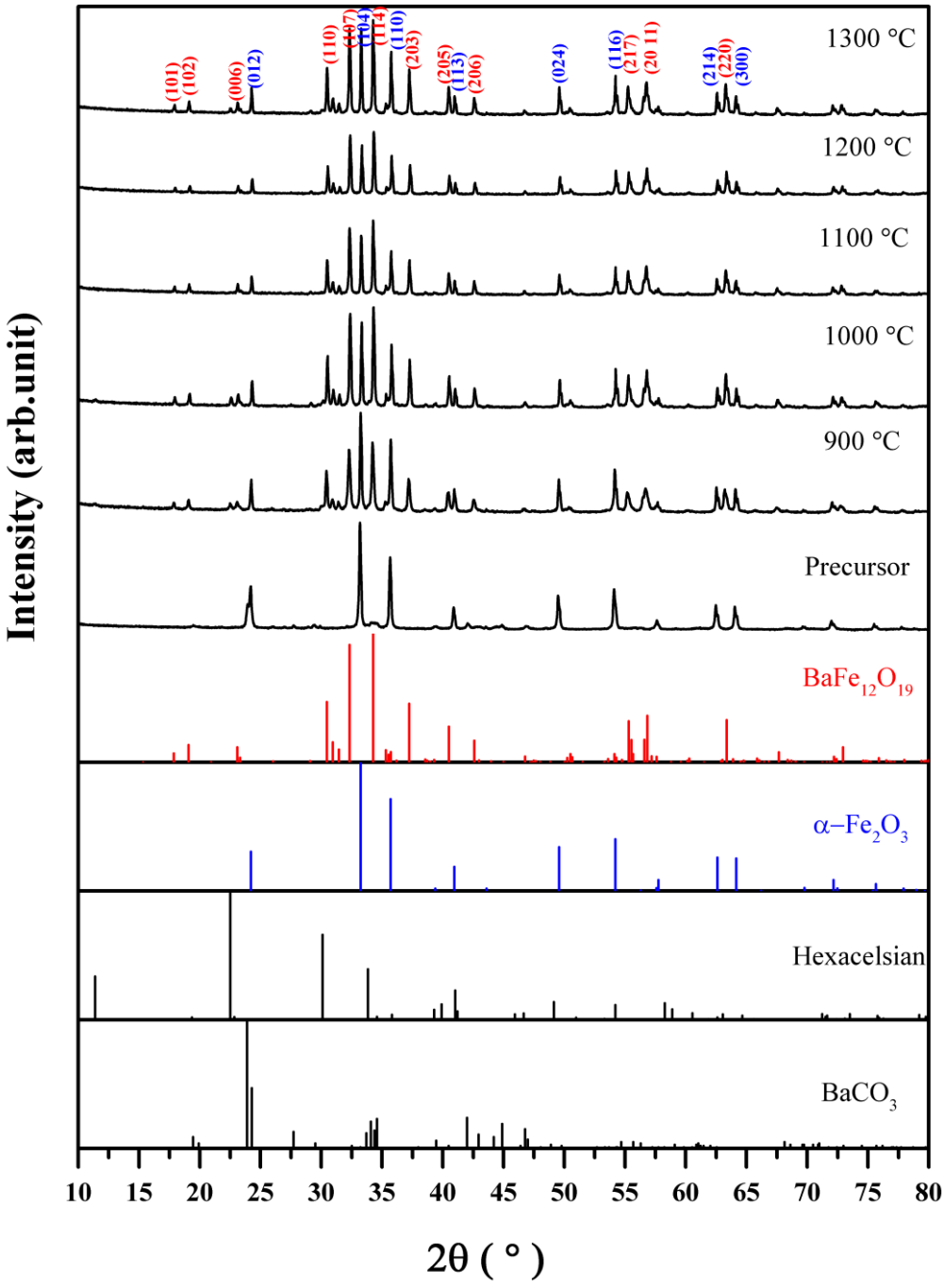

Figure S4. XRD patterns of A_1F before and after calcination at the target temperature for 4 h. The standard patterns retrieved from the database of the ICDD include $BaFe_{12}O_{19}$ (PDF 00-043-0002), α-Fe_2O_3 (PDF 01-079-0007), hexacelsian ($BaAl_2Si_2O_8$, PDF 01-072-7502), and $BaCO_3$ (PDF 00-044-1487).

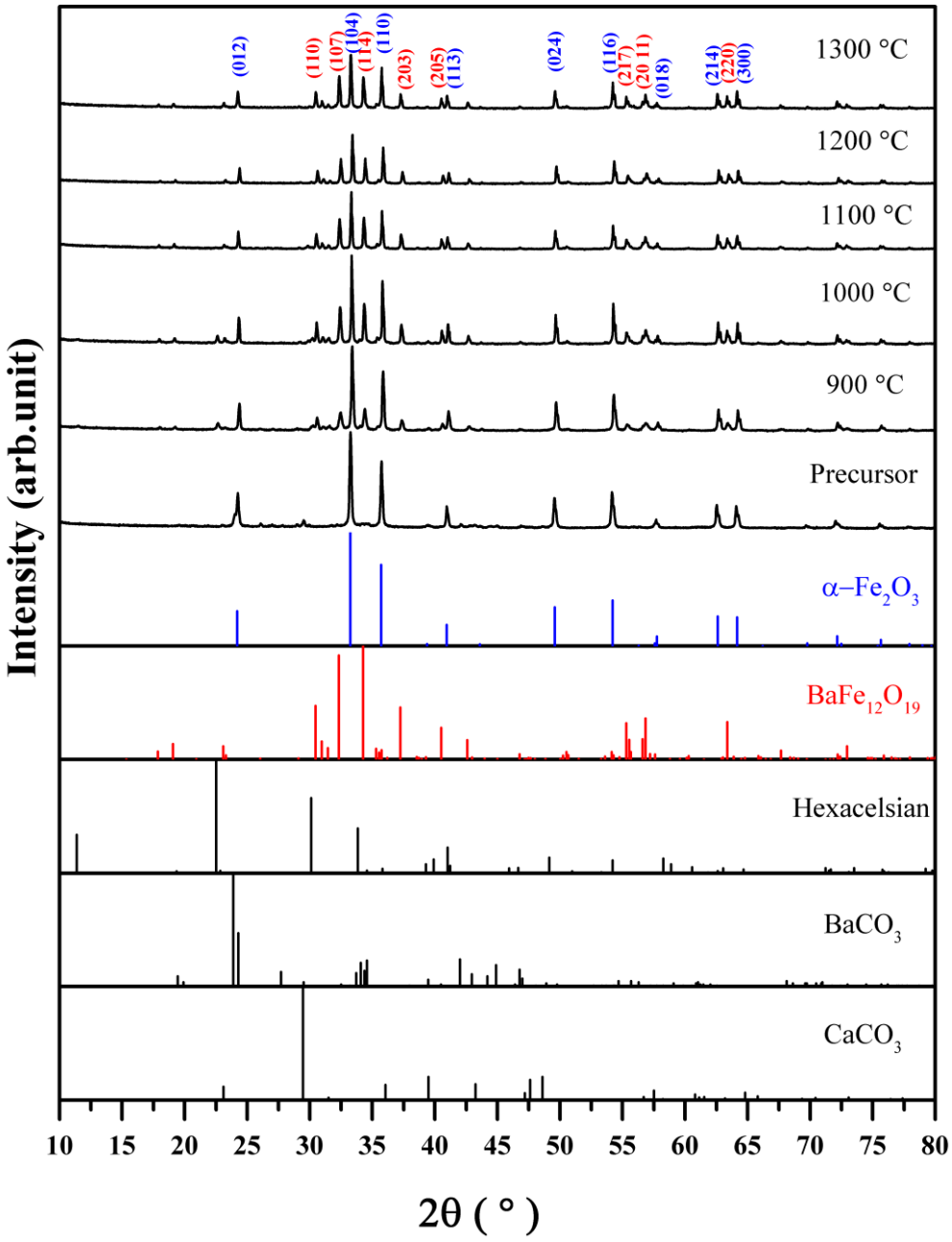

Figure S5. XRD patterns of A_2F before and after calcination at the target temperature for 4 h. The standard patterns retrieved from the database of the ICDD include $BaFe_{12}O_{19}$ (PDF 00-043-0002), α-Fe_2O_3 (PDF 01-079-0007), hexacelsian ($BaAl_2Si_2O_8$, PDF 01-072-7502), $BaCO_3$ (PDF 00-044-1487), and $CaCO_3$ (PDF 01-085-0849).

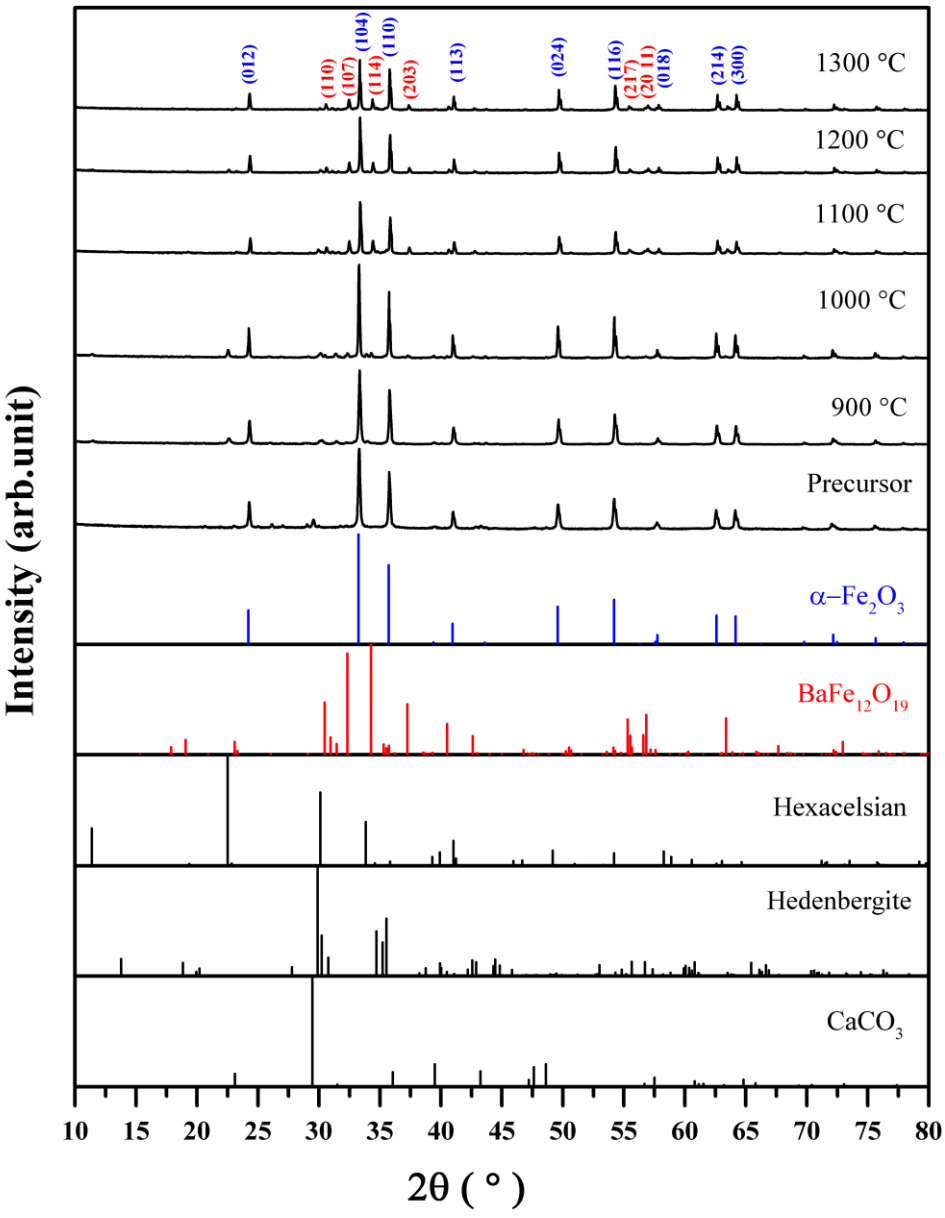

Figure S6. XRD patterns of A_3F before and after calcination at the target temperature for 4 h. The standard patterns retrieved from the database of the ICDD include $BaFe_{12}O_{19}$ (PDF 00-043-0002), α-Fe_2O_3 (PDF 01-079-0007), hexacelsian ($BaAl_2Si_2O_8$, PDF 01-072-7502), hedenbergite aluminian ($Ca(Fe_{0.821}Al_{0.179})(SiAl_{0.822}Fe_{0.178}O_6)$, PDF 01-078-1546), and $CaCO_3$ (PDF 01-085-0849).

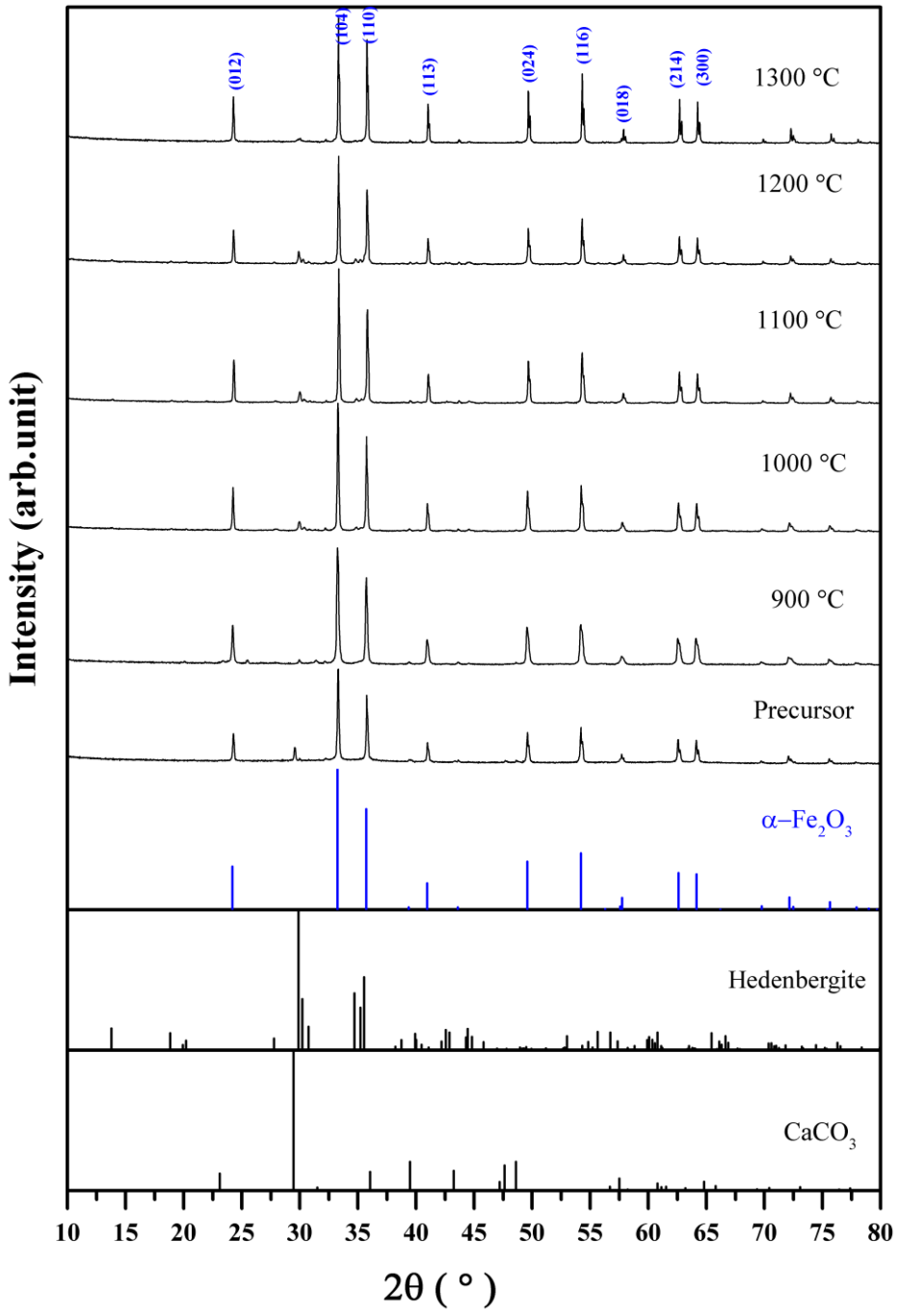

Figure S7. XRD patterns of A_4F before and after calcination at the target temperature for 4 h. The standard patterns retrieved from the database of the ICDD include α-Fe_2O_3 (PDF 01-079-0007), hedenbergite aluminian ($Ca(Fe_{0.821}Al_{0.179})(SiAl_{0.822}Fe_{0.178}O_6)$, PDF 01-078-1546), and $CaCO_3$ (PDF 01-085-0849).

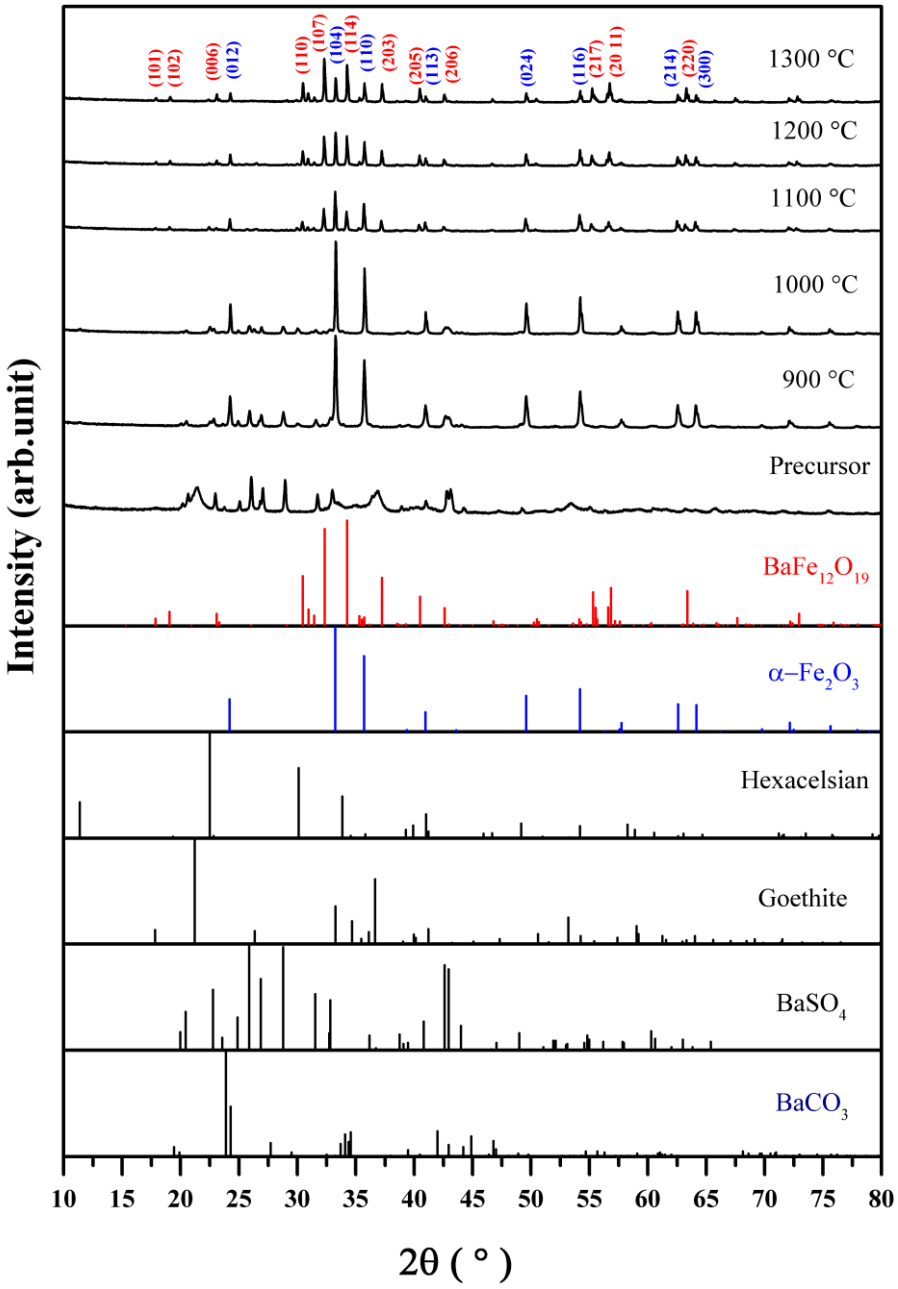

Figure S8. XRD patterns of A_0B before and after calcination at the target temperature for 4 h. The standard patterns retrieved from the database of the ICDD include $BaFe_{12}O_{19}$ (PDF 00-043-0002), α-Fe_2O_3 (PDF 01-079-0007), hexacelsian ($BaAl_2Si_2O_8$, PDF 01-072-7502), goethite (α-FeOOH, PDF 01-076-7156), $BaSO_4$ (PDF 00-005-0448), and $BaCO_3$ (PDF 00-044-1487).

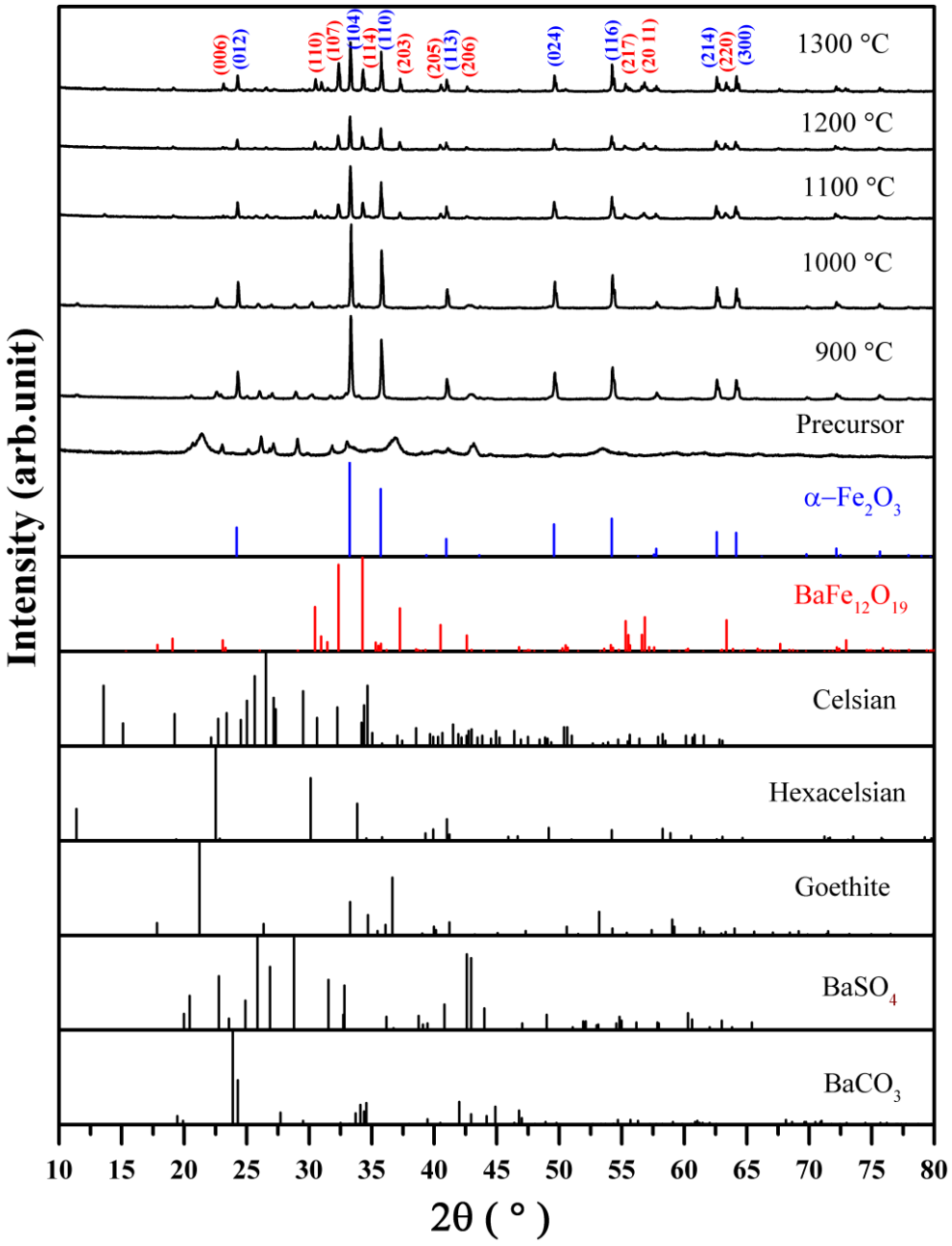

Figure S9. XRD patterns of A_1B before and after calcination at the target temperature for 4 h. The standard patterns retrieved from the database of the ICDD include $BaFe_{12}O_{19}$ (PDF 00-043-0002), α-Fe_2O_3 (PDF 01-079-0007), celsian ($BaAl_2Si_2O_8$, PDF 00-038-1450), hexacelsian ($BaAl_2Si_2O_8$, PDF 01-072-7502), goethite (α-FeOOH, PDF 01-076-7156), $BaSO_4$ (PDF 00-005-0448), and $BaCO_3$ (PDF 00-044-1487).

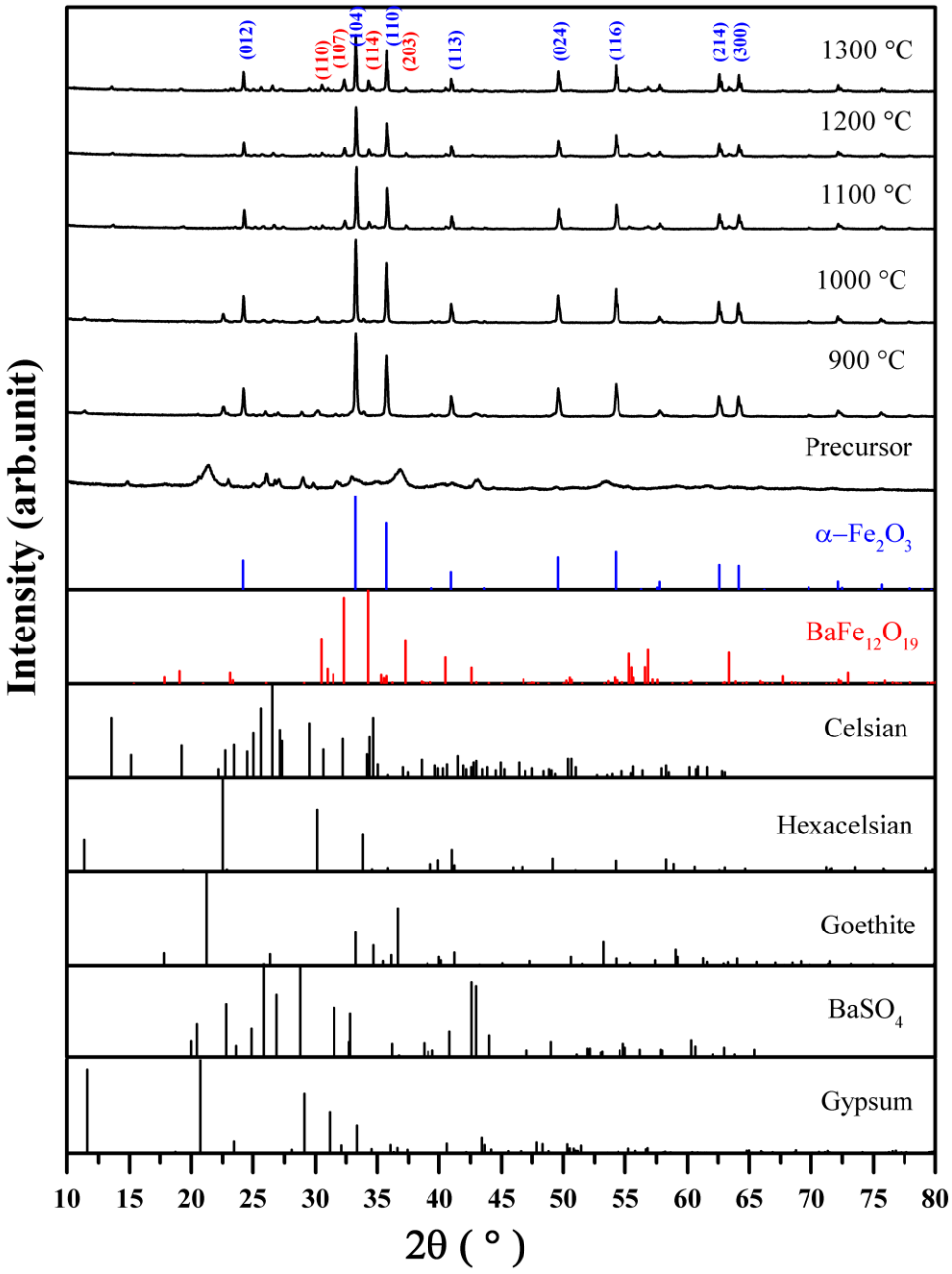

Figure S10. XRD patterns of A_2B before and after calcination at the target temperature for 4 h. The standard patterns retrieved from the database of the ICDD include $BaFe_{12}O_{19}$ (PDF 00-043-0002), α-Fe_2O_3 (PDF 01-079-0007), celsian ($BaAl_2Si_2O_8$, PDF 00-038-1450), hexacelsian ($BaAl_2Si_2O_8$, PDF 01-072-7502), goethite (α-FeOOH, PDF 01-076-7156), $BaSO_4$ (PDF 00-005-0448), and gypsum ($CaSO_4{\cdot}(H_2O)_2$, PDF

01-070-0983).

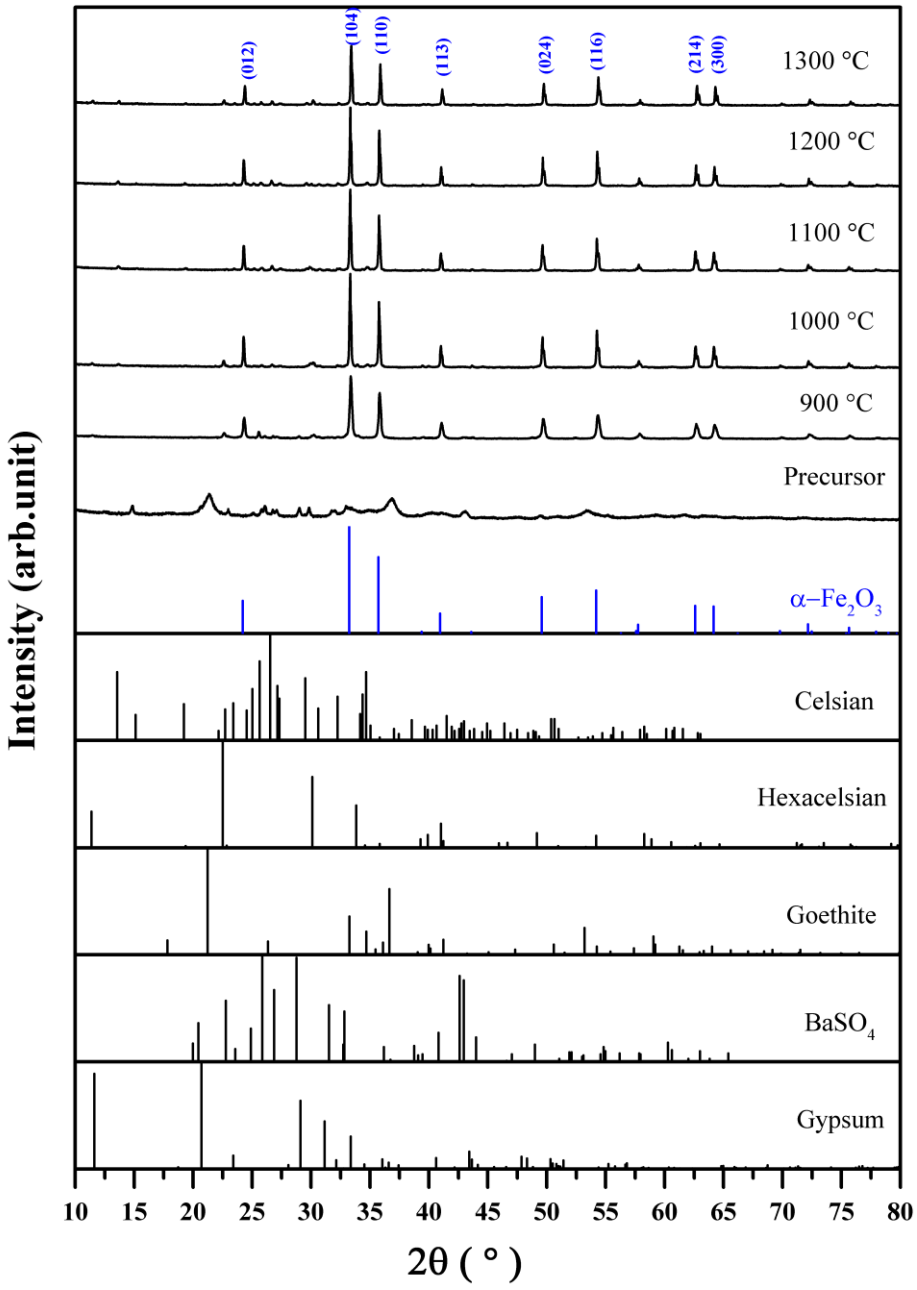

Figure S11. XRD patterns of A_3B before and after calcination at the target temperature for 4 h. The standard patterns retrieved from the database of the ICDD include α-Fe_2O_3 (PDF 01-079-0007), celsian ($BaAl_2Si_2O_8$, PDF 00-038-1450), hexacelsian ($BaAl_2Si_2O_8$, PDF 01-072-7502), goethite (α-FeOOH, PDF 01-076-7156), $BaSO_4$ (PDF

00-005-0448), and gypsum ($CaSO_4·(H_2O)_2$, PDF 01-070-0983).

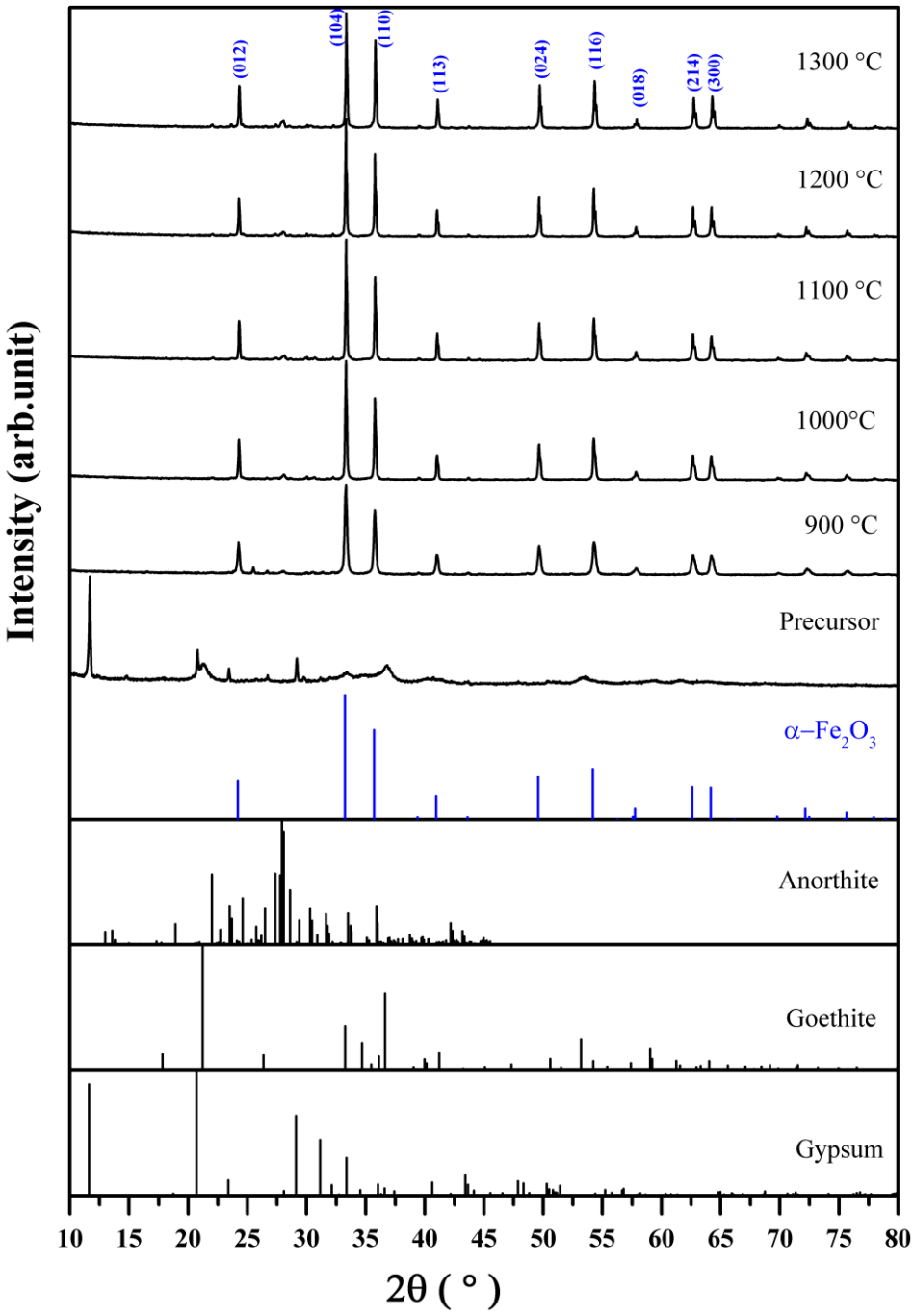

Figure S12. XRD patterns of A_4B before and after calcination at the target temperature for 4 h. The standard patterns retrieved from the database of the ICDD include α-Fe_2O_3 (PDF 01-079-0007), anorthite ($CaAl_2Si_2O_8$, PDF 01-075-1587), goethite (α-FeOOH,

PDF 01-076-7156), and gypsum ($CaSO_4 \cdot (H_2O)_2$, PDF 01-070-0983).